Chapter 15
Pulverisation of Emulsions with Supercritical CO_2

Pavlinka Ilieva, Andreas Kilzer, and Eckhard Weidner

Abstract With the use of a carbon dioxide-assisted high pressure spraying process, it is possible to manufacture solid emulsions with or without the employment of surfactants. Depending on the process parameters, such as spray pressure, temperature, and gas-to-liquid ratio, various powder morphologies and sizes in the range of micrometers can be obtained. The aim of the project is to investigate and compare the fundamental differences in the spray formation mechanisms of this process to the conventional ones. To this end, firstly various high pressure thermo- and fluid dynamic data have been investigated to define the process and identify different effects coming from the liquid's properties. Two model emulsions, water, and tristearin (water in oil) and rapeseed oil and polyethylene glycol (oil in water) have been chosen. Using a pseudo shadowgraphy technique spraying experiments with pure and gas-saturated liquids as well as the emulsions have been carried out with a flat fan orifice. The images of the sprays illustrate that the carbon dioxide generally leads to an earlier sheet breakup by gas nucleation. An increase in saturation pressure led to atomisation directly after the nozzle for rapeseed oil and tristearin. A decrease in breakup length of the liquid sheet was also observed for the water in oil emulsion. Solid emulsion particles were also produced in the range of 10 μm with various concentrations of the dispersed phase. It was shown that these can be produced without the use of an emulsifier. Moreover through the employment of an optical chamber, the encapsulation efficiency of the process was linked to the quality of the emulsion, that is size of dispersed droplets.

P. Ilieva • A. Kilzer
Chair of Process Technology, Ruhr University Bochum, Bochum, Germany

E. Weidner (✉)
Chair of Process Technology, Ruhr University Bochum, Bochum, Germany

Fraunhofer Institute UMSICHT, Oberhausen, Germany
e-mail: eckhard.weidner@umsicht.fraunhofer.de

U. Fritsching (ed.), *Process-Spray*, DOI 10.1007/978-3-319-32370-1_15

15.1 Introduction

The interest in supercritical fluids and their usage in various industrial processes has been on the rise in the past few decades. Their applications are widely ranged and vary from the food and pharmaceutical to material and waste industry. Special attention has been paid to their use in spraying processes as they are proving to be suitable for powder production [1–3]. An extensive research more recently shows that they meet the requirements for the production of carrier materials for active substances, extending their application to the production of microcapsules and composite materials [4]. Their advantages lie mainly in the production of solvent free powders, adjustable particle sizes, and lower process temperatures for thermolabile substances. Moreover, the product properties can be easily adjusted by variation of the process parameters.

Carbon dioxide has been the supercritical fluid of choice for many high pressure spraying processes. It proves to be beneficiary in this application as a variation of the spraying pressure, for example results directly in a change of the thermophysical properties of the substances to be sprayed. Moreover, most of these processes take advantage of the high gas solubility in the liquids. In the used CO_2-assisted high pressure spraying process, 20–30 wt% gas is usually dissolved in the liquid substance. The viscosity and interfacial tension are amongst the most affected properties hereby, with values reducing to more than 50 %. By making use of the more favourable properties of the CO_2-saturated liquids, it was assumed possible to produce solid emulsions which are not only solvent free, but also free of surface active agents which are inevitable for most common processes. Therefore, in the scope of this work new opportunities were explored with the given process in the field of emulsification and encapsulation. Knowing how the mechanisms of spray formation are affected by changes in their most influential properties makes the direct influence on the powder characteristics possible. However, a lack of knowledge exists on the effects of high concentrations of dissolved gasses on the disintegration mechanisms, as processes as gas nucleation in the liquid sheet or jet, which is assumed to govern the droplet formation mechanism have not been thoroughly investigated. The overall aim of this work is to gain a deeper understanding of the particle formation mechanisms and the possibilities of their manipulation for the production of tailor made particles.

15.2 Materials

Tristearin was supplied by Cremer Oleo GmbH & Co. KG and commercially available rapeseed oil was purchased from a local shop. The used tristearin has a melting point of 72 °C. Both triglycerides were used without further treatment. Polyethylene glycol 400 was purchased from Sigma Aldrich, while polyethylene glycol 2000 and 6000 were provided by Clariant. PEG 400 is liquid at room temperature, whereas PEG 2000 and 6000 are solids with melting points of

ca. 50 °C and 63 °C, respectively. The water used for all experiments was taken from a tap and purified using the PURELAB flex from ELGA which resulted in type I ultrapure water. The used carbon dioxide (CO_2) was supplied by YARA Industrial GmbH and had a purity of 99.9 vol.%. Nitrogen (N_2) with a purity of 99.9 vol.% was supplied by Air Liquide Deutschland GmbH. The two non-ionic emulsifiers, sorbitane monooleate (Span® 80) and polyethylene glycol sorbitane monooleate (Tween® 80) were purchased from Sigma Aldrich and were used without further treatment.

15.3 Thermodynamic Properties of the Investigated Liquids

15.3.1 Experimental Procedures

15.3.1.1 Solubility Measurements

The static analytic method with sampling was used for the vapour liquid equilibrium measurements using a variable volume view cell (New Ways of Analytics, Germany) presented in Fig. 15.1.COMP: Please maintain Figure citation as per the MS in order to maintain sequence for reference citation.OK.

The stainless steel high-pressure view cell (D-2) is equipped with two sapphire windows, placed in the front and rear of the cell's body. This allows visualisation of the cell's interior and therefore also qualitative investigation of phase behaviour. The rear sapphire is connected to a pneumatic hydraulic piston (C-1). During sampling the piston moves forward, minimising the cell's volume and thereby ensuring a constant pressure. The view cell has a volume of 54 cm^3, which can

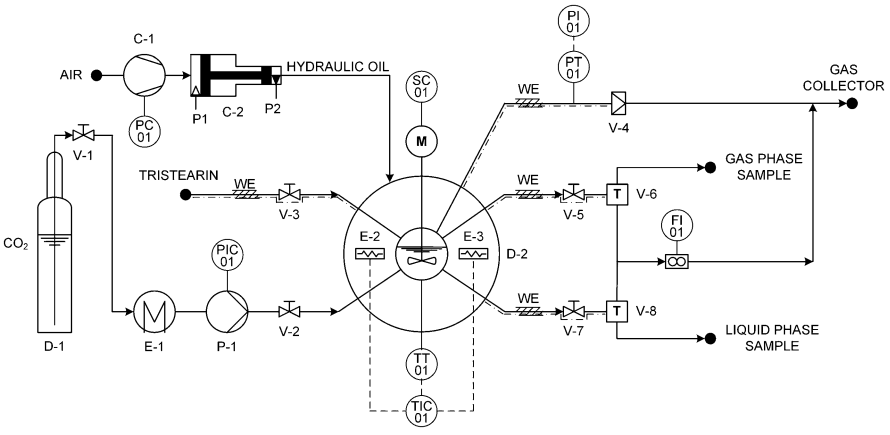

Fig. 15.1 Schematic flow chart of the high-pressure view cell used for the phase equilibria measurements

be reduced to 24.7 cm^3 and is designed for a maximum pressure of 75 MPa and a temperature of 473 K.

At the commencement of each experiment the cell was thoroughly cleaned to ensure that no residues from previously used substances were present. It was then heated to the desired temperature with two cartridge heaters (E-2 and E-3, HORST GmbH, Germany), incorporated into two holes of the cell's body. The temperature was measured and controlled by a K-Type thermocouple (TT 01, ±1 °C), connected to a controller (TIC 01, MC1-10A, HORST GmbH, Germany). After the desired temperature was reached, the cell was filled with the liquid sample to about half of its volume. The exact amount of liquid sample or carbon dioxide used for the experiment must not be previously known for the sampling method. Prior to the cell's pressurisation, it was purged with carbon dioxide to remove air. Afterwards, it was filled with carbon dioxide to the desired pressure by a high-pressure pump (P-1) equipped with cooler (E-1, New Ways of Analytics, Germany). The pressure was monitored using a digital pressure transmitter (PT 01, ±0.5 %, S-11, WIKA, Germany). To avoid apparatus damage in the case of the maximum operating pressure being exceeded, the view cell is equipped with a rupture disc with a rupture pressure of 60 MPa at 293 K (V-4).

To ensure proper mixing of the substances, a magnetic stirrer (M) coupled to a power supply unit (SC 01) was used. Initially, a significant pressure drop could be observed as a result of the dissolving CO_2, which was compensated for by introducing more gas in the view cell. A mixing time of 1 h, followed by a rest time of minimum 2 h was set for all experiments. These times were determined in previous investigations. As a result of density difference, the resulting two phases in the cell had fully separated. An observation of the equilibrium state was carried out to make sure that no bubbles were present in the heavy phase and there were no droplets in the light phase. Isothermal and isobaric conditions were maintained during the whole experiment.

Once equilibrium was reached, at least two samples of each of the phases were taken. A valve was connected to the upper part of the cell for the light phase (V-6) and the bottom part for the heavy phase (V-8). The samples were collected and contained in glass test tubes. Due to the significant pressure gradient between the cell and the test tubes, the samples underwent degasification. Glass traps were therefore necessary to redirect the gas to a volumetric gas meter (FI 01, $\pm 10^{-6}$ m^3, ELSTER Group GmbH, Germany,). The sampling was carried out without disturbing the equilibrium, that is the pressure was held constant while the volume was minimised by moving the rear sapphire forward. The maximum pressure variation observed during sampling was ±0.2 MPa. All measurement points were repeated twice.

15.3.1.2 Viscosity and Density Measurements

The viscosity and density of the gas-saturated liquids of the binary systems investigated were measured simultaneously using a frequency oscillator from Schwing Verfahrenstechnik GmbH, Germany (Fig. 15.2). The apparatus is based on the

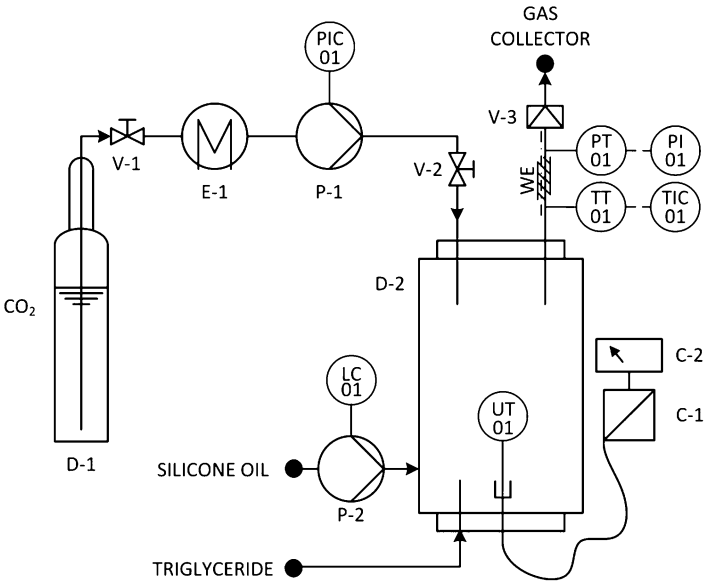

Fig. 15.2 Schematic flow chart of the high-pressure autoclave used for the viscosity and density measurements

oscillating U-tube principle, which, ever since its first implementation for density measurements in 1967 by Anton Paar, has become a standard for modern day digital density meters. Instead of a U-tube, the apparatus used in this work has the shape of a tuning fork, with a piezo crystal built into the top of each tine. Quartz crystals are used given their superior properties. One of the piezo crystals is used to set the oscillator in a vibrating motion, the other for measuring the equivalent resonance frequency. An oscillator completely submerged in a fluid, vibrates at a resonance frequency, which differs from the natural frequency of the oscillator in a vacuum and is directly dependant on the difference in density between the fluid and the oscillator [5]. On the other hand, the vibration of the oscillator causes a shear wave through the fluid, which is damped due to the fluid's viscosity. The viscous drag created on the surface of the oscillator also influences the resonance frequency, requiring an amplifier to keep the frequency constant [6]. By measuring the cut-off frequencies of the vibration at a given amplitude (−3 dB), and thereby the bandwidth of the oscillation, the equivalent vibration periods can be calculated. These allow the calculation of the viscosity of the surrounding fluid [7].

The frequency oscillator was incorporated in the bottom lid of a high-pressure autoclave (D-2) from Innoweld Metallverarbeitung GmbH, Austria. The autoclave is designed for a maximum pressure of 20 MPa, maximum temperature of 473 K and has a volume of 1.7 dm^3. The autoclave is heated using a double jacket connected to a silicone oil-circulating thermostat (P-2), Lauda Proline Edition X, Germany. The temperature is measured at two positions inside the autoclave. A K-type thermocouple (TT 01) is placed in the top lid of the autoclave, showing the

temperature of the light phase during measurements and a Pt-100 resistance thermometer is located inside the frequency oscillator (UT 01), monitoring the temperature of the dense phase. The pressure was controlled by a digital pressure transducer (PT 01, ±0.5 %, S-11, Wika, Germany). The autoclave and its stand are designed to enable shaking so that the required time for phase equilibria can be reduced. The frequency oscillator is connected to a measuring converter (C-1) on whose display the values of viscosity, density and temperature can be read (C-2).

At the beginning of each experiment, the autoclave and frequency oscillator were thoroughly cleaned to remove residues from previous experiments. According to the manufacturer, at least 0.6 dm^3 of liquid is required to perform a measurement. This ensures that the oscillator is completely covered by the liquid being investigated. For the experiments, a minimum of 0.7 dm^3 per experiment was used. After the liquid was introduced, the autoclave was flushed with CO_2 to remove air and subsequently pressurised with the high-pressure liquid CO_2 pump (P-1) equipped with a cooler (E-1). After reaching the desired pressure, the autoclave was shaken for ca. 5 min to enhance the mixing of the substances. This resulted in a high pressure drop, which required the autoclave to be refilled with CO_2. This procedure was repeated a small number of times. Subsequently, a shaking time of 1 h, followed by a 2 h resting time was set for all experiments. This allowed for the phases to separate. Once the phases were separated, the values for the viscosity, density and temperature were noted.

The viscosity of the liquids at ambient pressure was measured using a rotational viscometer (RS75, Haake, Germany). Both liquids, tristearin and rapeseed oil, show Newtonian flow behaviour and therefore differences in the shear rate between the two measuring devices do not influence the viscosity values.

The density of the liquids at ambient pressure was measured using a hydrometer (Schneider GmbH, Germany).

Each viscosity and density experiment was carried out three times.

15.3.1.3 Interfacial Tension Measurements

The interfacial tension of CO_2-saturated triglycerides in a triglyceride-saturated CO_2 atmosphere was measured using the pendant drop method introduced in 1938 by Andreas et al. [8]. In this method, a drop is suspended on a capillary in a gas or liquid atmosphere. Its shape results from the balance of gravitational and interfacial forces. As the drop minimises its surface by taking on spherical shape, the pressure inside the drop increases as a result of the curved interface. At the same time, the spherical shape is distorted under the weight of the drop. This results in pear-shaped droplets, which are typical for this method.

A combination of two view cells and a DSA 100 measuring apparatus from Kruess GmbH, Germany was used as presented in Fig. 15.3. Since the Drop Shape Analyser instrument is designed by the manufacturer for measurements at atmospheric pressure only, a high-pressure view cell (D-3) was placed between the camera (K-1) and light source (L-1) of the DSA 100, so that measurements under high pressure would also be possible. This cube-shaped stainless steel view cell is

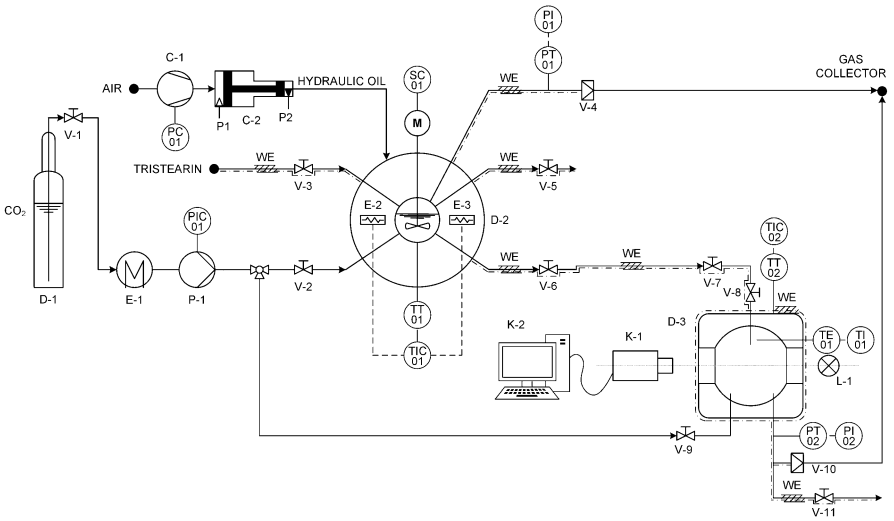

Fig. 15.3 Schematic flow chart of the apparatus used for the interfacial tension measurements

designed for a maximum operating pressure of 20 MPa and temperature of 473 K. On two opposite sides borosilicate windows are screwed in, allowing observation of the spherically shaped cell's interior. The pressure was controlled using a digital pressure transducer (PT 02, ±0.5 %, S-11, Wika, Germany). The heating of the view cell is achieved by electric rope heaters controlled by a K-type thermocouple (TT 02) connected to a controller (TIC 02, ±0.25 %, MC1 10, Horst GmbH, Germany). The capillary used to position a droplet was introduced from the cell's top and a second temperature measuring element (TE 01) placed in the vicinity of the droplet was screwed in from the side. Previous authors have shown the importance of measuring the temperature as closely as possible to the droplet to avoid large errors in density coming from inaccurate temperature measurement [9]. A small change in temperature and pressure leads to a strong variation of the CO_2 density near the vapour pressure curve or the critical point. Hebach et al. [9] could show that this could be avoided by measuring the temperature close to the droplet rather than in the cell's wall. The capillary used was made of stainless steel (316 SS) and had an outside diameter of 1/16′ (Vici Valco, through Altmann Analytik GmbH & Co. KG, Germany). The capillary was connected through a micro-metering (V-7) and regulating valve (V-8) to the second view cell (D-2), which was used as a reservoir for the gas-saturated liquid. This high-pressure view cell is the same as the cell used to measure the solubility, except that it is designed for a maximum operating pressure of 45 MPa.

At the beginning of the experiments, the cells were thoroughly cleaned. The procedure described previously for the solubility measurements was followed to saturate the triglycerides with CO_2 in the high-pressure view cell. Before the mixing period was started the valves between the two cells were opened, so that some triglyceride could flow through the capillary into the second cell. This was done to ensure that the CO_2 atmosphere in the second cell was saturated with the

triglyceride and no diffusion effects between the CO_2 and the triglyceride droplet could be expected. After the phase equilibrium condition was reached, the valves were again opened and using the micro metering valve a single droplet was positioned at the top of the capillary. Using the Drop Shape Analyzer software, the measurement was then started. The software uses the Young-Laplace equation to calculate interfacial tension, after it has fitted the droplet profile by iteratively determining its curve radius. The Georgiadis et al. [10] method for the evaluation was followed. A photograph was taken and evaluated every 4 s over a period of 10 min. For a set of parameters, four droplets were investigated and each measurement was repeated once.

15.3.2 Results

15.3.2.1 Solubility

The high pressure equilibrium data for the investigated systems are presented in Figs. 15.4, 15.5, 15.6, 15.7, 15.8 and 15.9. The solubility results for CO_2 in the liquids show an increase with rising pressure and falling temperature. This is typical behaviour for carbon dioxide. In all cases, the miscibility gap does not close at the investigated temperatures and pressures. The influence of the pressure on the CO_2 solubility declines at higher values. This is usually correlated to the CO_2 density, which increases drastically in the near critical region. Further away from the critical temperature and pressure this effect diminishes and a near linear increase in density is reached. Except for water the CO_2 solubility in the liquids is relatively high with values exceeding 30 wt% at 25 MPa. On the contrary, the liquid solubility in the supercritical fluid barely reaches 1 wt% in most cases.

The binary system tristearin and CO_2 was investigated at four different temperatures, 343, 353, 363 and 373 K (Fig. 15.4). A maximum solubility value of 32.8 wt % was measured in the dense phase at 353 K and 25 MPa. The obtained results were

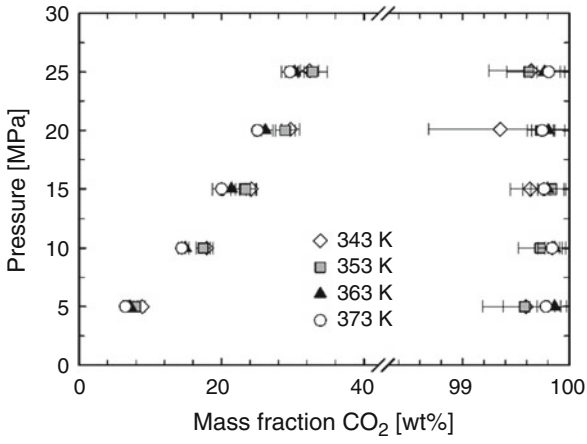

Fig. 15.4 Phase equilibria of tristearin and CO_2 at 343, 353, 363 and 373 K

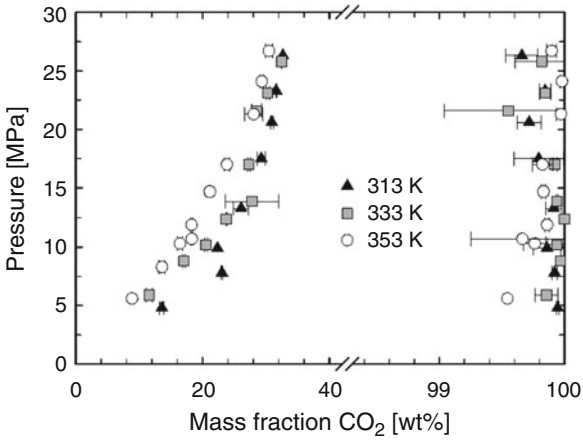

Fig. 15.5 Phase equilibria of rapeseed oil and CO_2 at 313, 333 and 353 K

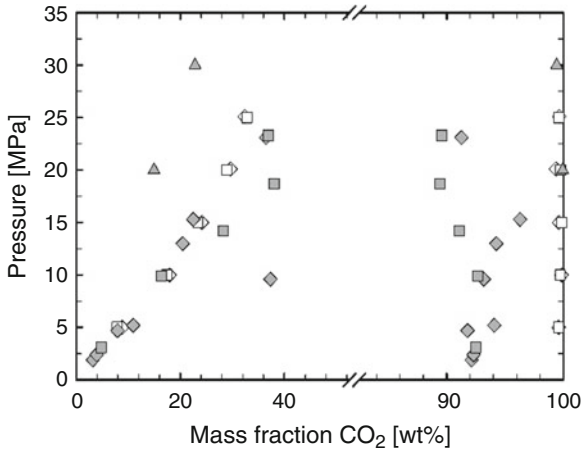

Fig. 15.6 Comparison of the solubility data for the system tristearin and CO_2 with literature data (*open square*) 343 K, (*open diamond*) 353 K, (*filled diamond*) 343 K [12], (*filled square*) 353 K [12] and (*filled triangle*) 353 K [11]

compared with available literature [11, 12] and are presented in Fig. 15.6. Given that Weber et al. [11] measured the phase equilibria across a very wide pressure range, only two points at higher pressure values can be compared. All of the results follow the same trend and show the same influence of temperature and pressure on the solubility. The values for the phase compositions obtained in this work lie between those noted in the literature. The solubility data from [12] show higher values but also greater scattering for both, the light and dense phase. The results from [11] show the lowest solubility data for both phases. According to the authors, Weber et al. [11] used tristearin with 90 wt% purity and Perko et al. [12] one with a melting point of 61 °C, which is an indication for lower purity. The fat used in this work has a melting point of 71 °C and according to the manufacturer, pharmacological purity. As impurities affect the physical properties of substances, it can be assumed that the solubility as such would also be affected. As mentioned in their

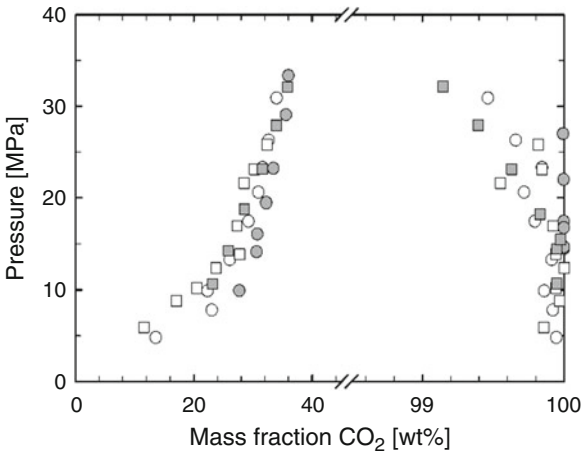

Fig. 15.7 Comparison of the solubility data for the system rapeseed oil and CO_2 with literature data (*open circle*) 353 K, (*open square*) 333 K, (*filled circle*) 313 K [14] and (*filled square*) 333 K [14]

papers, both authors used the static analytic method with sampling. Each method has its drawbacks and with the static analytic method the main error source comes from the sampling steps, so that small deviations in the results can be thereby accounted for. By always taking more than one sample for a specific set of parameters and repeating the experiments, at least once, high point scatter can be avoided [13].

The binary solubility data of rapeseed oil and carbon dioxide were measured at three different temperatures, 313, 333 and 353 K (Fig. 15.5). As mentioned before, the solubility of CO_2 in rapeseed oil also increases with rising pressure and falling temperature. The highest solubility of nearly 34 wt% was measured at 313 K and 30.9 MPa. The measured data was compared to literature [14] as depicted in Fig. 15.7. The results obtained in this work for 313 and 333 K show lower CO_2 solubility. These deviations are however relatively small (1–2 wt%), especially when taking into account that the rapeseed oil used is not a standardised product. Therefore, they can be explained with deviations in the composition of the vegetable oil [13].

The phase behaviour of PEG 2000 and CO_2 was investigated at 333 and 353 K and pressures up to 30 MPa. The binary system shows an open miscibility gap as presented in Fig. 15.8. The highest solubility of the supercritical fluid in the polymer melt of 29 wt% was measured at 33.2 MPa and 333 K. Similar to the other investigated liquids, the polymer dissolves only in small quantities in CO_2. At 333 K the highest measured solubility was 3 wt%, at 353 K only 0.2 wt%. Taking into account the typical uncertainty of 1 wt% of the used sampling method, no precise information can be given for the light phase composition.

The measured solubilities were compared to literature values for polyethylene glycols of different molar mass and carbon dioxide [17, 18]. The results are presented in Fig. 15.10. It can be observed that for polyethylene glycols the molar mass does not have a strong influence on the solubility of CO_2. Wiesmet observed that polyethylene glycols with molecular masses lower than 1500 g/mol

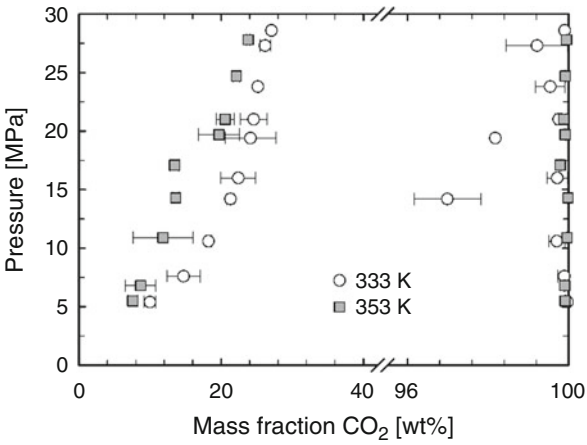

Fig. 15.8 Phase equilibria of PEG 2000 and CO_2 at 333 and 353 K

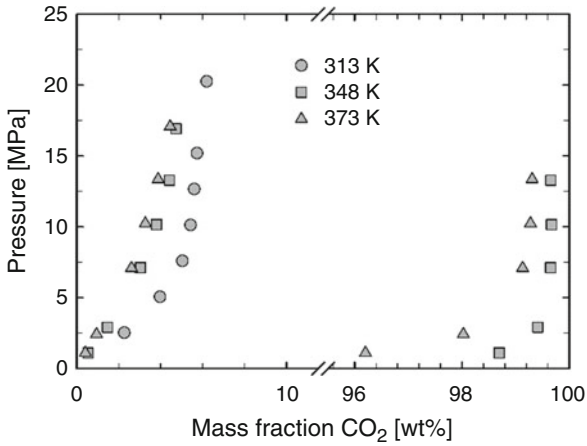

Fig. 15.9 Phase equilibria of water and CO_2 at 313 K [15], 348 and 373 K [16]

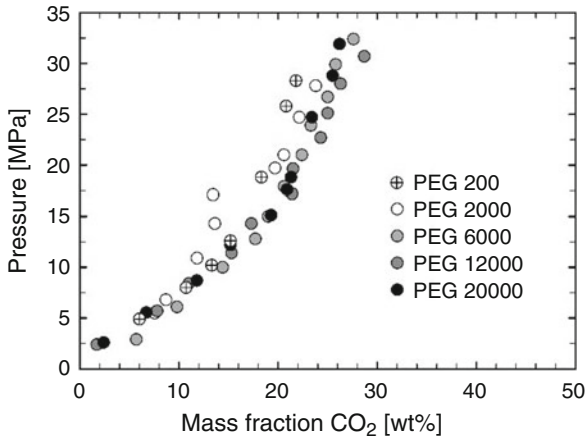

Fig. 15.10 Phase behaviour of polyethylene glycols of different molar masses and CO_2 at 353 K PEG 200 [18], PEG 6000–20000 [17]

show a slightly lower solubility for CO_2 only above 14 MPa in comparison to the ones with higher molar masses. One explanation offered by the authors is that with rising molar mass the ratio between hydroxyl and ethylene groups within the polymer chains falls. This leads to weakened polarity of the molecules causing only small differences in the phase behaviour of low and high molar mass polymers and carbon dioxide [17, 18].

The phase behaviour of water and carbon dioxide has been studied by various authors, so literature data in wide ranges of temperature and pressure is available. Selected data for the relevant pressure and temperature conditions are presented in Fig. 15.9 [15, 16]. CO_2 has the lowest solubility in water barely exceeding 6 wt% at 313 K and 20.3 MPa. The effect of pressure on solubility weakens above 5 MPa as depicted by the near vertical isotherm progress. The composition of the light phase shows around 4 wt% water vapour at 1.1 MPa and 373 K.

The influence of emulsifiers on the powder production and encapsulation efficiency will also be considered at a later stage in this project, so the phase behaviour between two non-ionic surfactants and carbon dioxide was also investigated as no literature data was available. The results are presented in Fig. 15.11 for Span® 80 and in Fig. 15.12 for Tween® 80.

Both emulsifiers show an open miscibility gap. The temperature seems to have a more pronounced effect in the lower pressure region for Span® 80 and carbon dioxide as the isotherms run closer to each other above 16 MPa. The highest CO_2-solubility in the emulsifier was measured at 333 K and 32.2 MPa. A maximum amount of 3.2 wt% emulsifier was found in the light phase at 353 K and 30 MPa. The effect of temperature can be observed clearly for the phase behaviour of Tween® 80 and carbon dioxide, where the isotherms only start approaching each other at pressures around 30 MPa. A maximum of 32.5 wt% of CO_2 was measured in the dense phase at 313 K and 30 MPa. Contrary to the relatively high gas solubility in the emulsifier, only less than 1 wt% of the viscous liquid could be found in the light phase in the investigated temperature and pressure range.

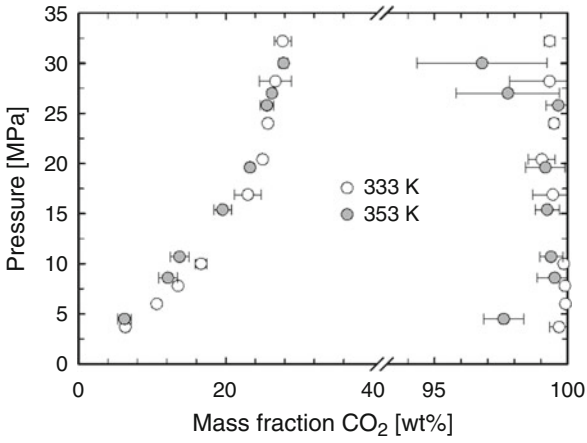

Fig. 15.11 Phase equilibria of Span® 80 and CO_2 at 333 and 353 K

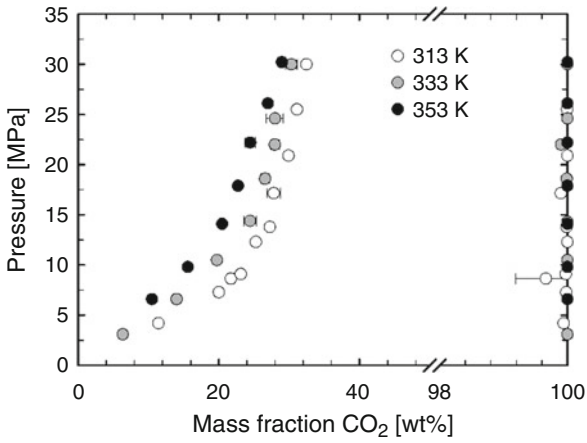

Fig. 15.12 Phase equilibria of Tween® 80 and CO_2 at 313, 333 and 353 K

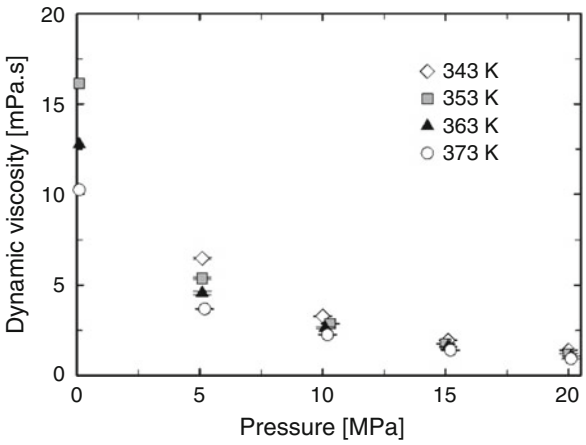

Fig. 15.13 Viscosity of CO_2-saturated tristearin at 343, 353, 363 and 373 K

15.3.2.2 Viscosity

The viscosity data for the triglycerides and carbon dioxide determined in this work are presented in Figs. 15.13 and 15.14. Available literature data for the polymers and carbon dioxide [19, 20] and water, pure [21] and saturated with CO_2 [22] are presented in Figs. 15.16 and 15.17, respectively.

Viscosity measurements at atmospheric pressure show a Newtonian behaviour for both tristearin and rapeseed oil. Unfortunately, varying or pre-setting the shear rate for the measurements using the high-pressure apparatus was not possible, so no specific information regarding it can be given. According to the manufacturer, the measurements are carried out at a shear rate between 0 and 100 s^{-1}.

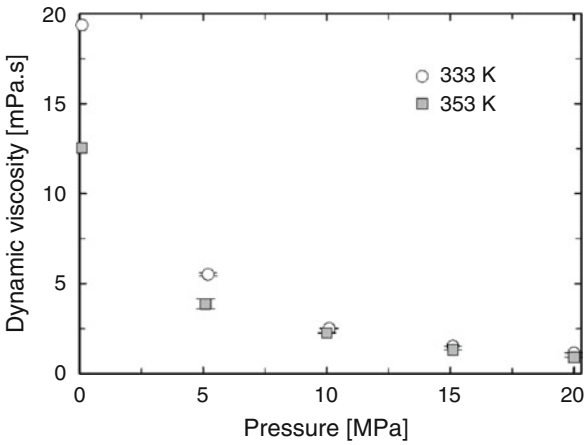

Fig. 15.14 Viscosity of CO_2-saturated rapeseed oil at 333 and 353 K

According to the results, both temperature and pressure influence the viscosity of the gas-saturated liquids. Measurements at atmospheric pressure using the Haake Rheostress RS75 have shown an exponential decrease of viscosity with rising temperature. This is in compliance with results from other authors for vegetable oils and fatty acids [23–25]. A comparison of the viscosity data for rapeseed oil at atmospheric pressure is also in good agreement with the literature [25]. However, the effect of temperature on viscosity with increasing pressure weakens, as with rising temperature the CO_2 solubility decreases, what was demonstrated above with the vapour liquid equilibrium data. As the opposite is true for the pressure, a significant decrease in viscosity was achieved for triglycerides with increasing saturation pressure. The experiments in this work have been carried out up to a maximum pressure of 20 MPa. At 353 K, the viscosity of CO_2-saturated tristearin decreased from initial 16.13 to 1.2 mPa s at 20 MPa. As a comparison at 373 K, the viscosity changed from initial 10.25 to 0.92 mPa s. The viscosity of rapeseed oil was reduced from 19.14 mPa s at atmospheric pressure and 333 K to 1.14 mPa s at 333 K and 20 MPa. Both triglycerides show a decrease in the viscosity with increase in pressure and temperature. The highest decrease in viscosity, 94 %, was determined in rapeseed oil at 20 MPa and 333 K. From Figs. 15.13 and 15.14, it can be seen that the viscosity values had not settled until a pressure of 20 MPa, although all values at this pressure are around 1 mPa s, independent of temperature. Viscosity data for canola [26] and fish oil [27] as well cocoa butter [28] from the literature have been compared in Fig. 15.15. The data show good agreement although the results from this work show slightly lower values for the viscosity of tristearin as well as rapeseed oil. The rheological behaviour of canola oil and fish oil are measured with a rotational rheometer, and cocoa butter with falling body viscometer. Small differences in the measured values can be contributed to the different type of viscometer used. Moreover, rheological measurements carried out by several authors [26, 27, 29] with CO_2-saturated oils all show shear thickening behaviour. Taking into account that the literature data for fish and canola oil have been determined at a

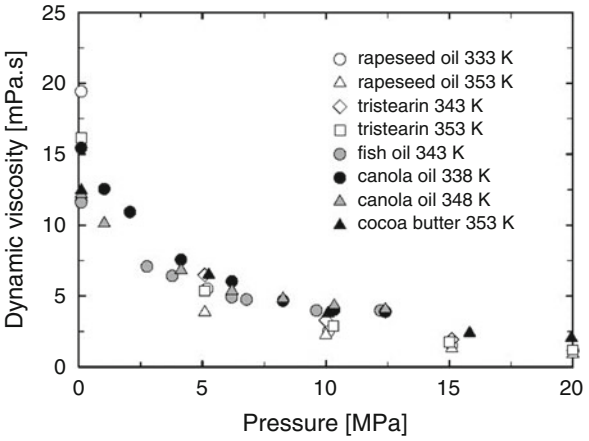

Fig. 15.15 Comparison of the viscosity of tristearin and rapeseed oil with literature values for fish oil [27], canola oil [26] and cocoa butter [28]

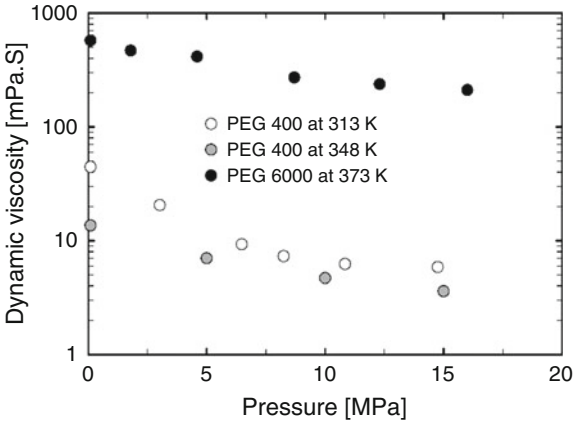

Fig. 15.16 Viscosity of CO_2-saturated PEG 400 at 313 and 348 K [20] and CO_2-saturated PEG 6000 at 373 K [17]

shear rate of 300 s^{-1} and because, as previously stated, the apparatus in this work covers shear rates between 0.1 and 100 s^{-1}, the difference in the values can be contributed to the dilatant behaviour of CO_2-saturated vegetable oils.

Selected data from the literature for the viscosities of CO_2-saturated PEG 400 [20] and PEG 6000 [17] (Fig. 15.16) show a decrease in the viscosity with rising temperature and pressure. A nearly 63 % reduction in viscosity was achieved for the higher molar mass polyethylene glycol at a pressure of only 16 MPa at 373 K, whereas for PEG 400 at 313 K and 14.8 MPa the viscosity reduced by 87 %.

The viscosity of water is only slightly influenced by the dissolved carbon dioxide as shown in Fig. 15.17 for 293 K [22]. A comparison with literature data for pure water [21] at 293 K show that with increasing pressure the viscosity of CO_2-saturated water rises. Dittmar explains that the ions formed by the CO_2 dissolution in water (HCO_3-, H+, OH−) have a reinforcing effect on the molecular structure

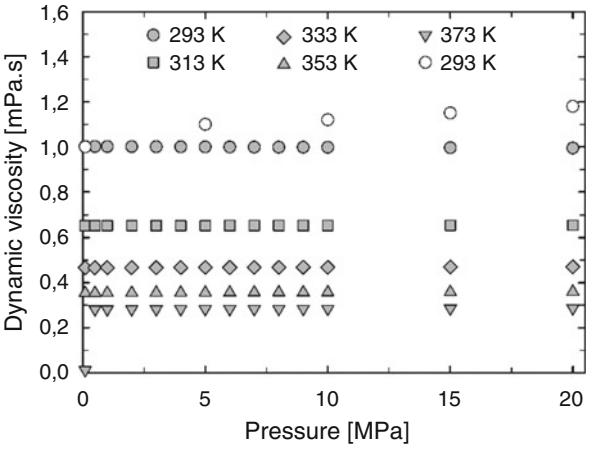

Fig. 15.17 Viscosity of pure water at different temperatures (*closed symbols*) [21] and CO_2-saturated water at 293 K (*open symbols*) [22]

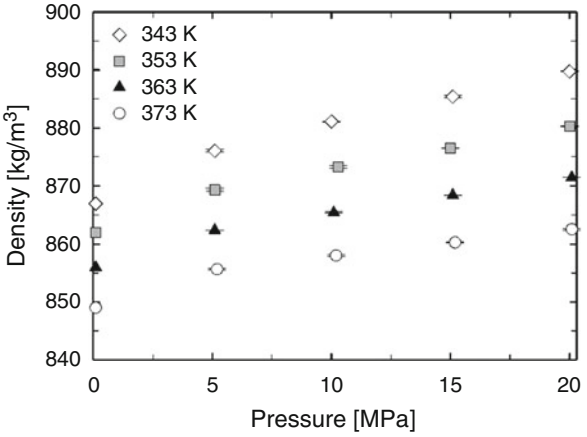

Fig. 15.18 Density of CO_2-saturated tristearin as a function of pressure at 343, 353, 363 and 373 K

of water and thereby could lead to a viscosity increase, the same effect being promoted through the dissolved polar molecules, H_2CO_3 [22]. Moreover, the hereby caused change in viscosity is negligible and further on in this work only the values for pure water are considered.

15.3.2.3 Density

The densities of tristearin and rapeseed oil saturated with CO_2 at 343, 353, 363, 373 K and 333 and 353 K, respectively and pressures of up to 20 MPa are presented in Figs. 15.18 and 15.19. Available literature data for the different polyethylene glycols [20, 30] and water [22] are presented in Figs. 15.22 and 15.23. A linear increase in density was observed for the investigated substances.

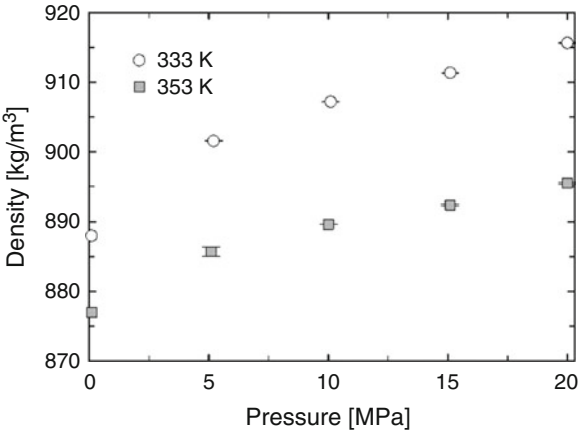

Fig. 15.19 Density of CO_2-saturated rapeseed oil as a function of pressure at 333 and 353 K

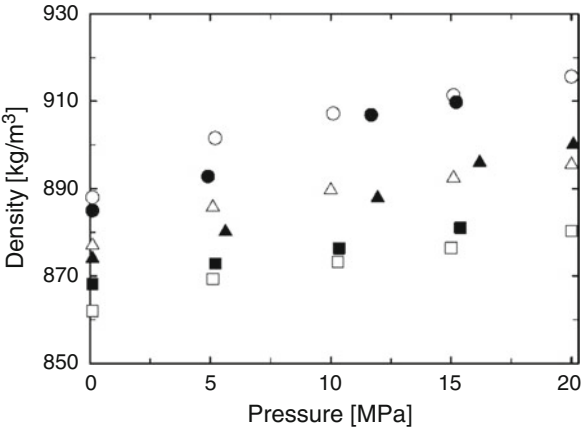

Fig. 15.20 Density of different triglyceride mixtures as a function of pressure: (*open square*) 353 K tristearin, (*open circle*) 333 K rapeseed oil, (*open triangle*) 353 K rapeseed oil, (*filled circle*) 333 K corn oil [32], (*filled triangle*) 351 K corn oil [32] and (*filled square*) 353 K cocoa butter [28]

The density of tristearin increased from 867 kg/m^3 at atmospheric pressure to 889.7 kg/m^3 at 20 MPa and 343 K. The smallest change in density was observed at 373 K where the density for the tristearin increased from 849 to 862.5 kg/m^3. For rapeseed oil, the density increased from 888 kg/m^3 at atmospheric pressure to 915.6 kg/m^3 at 20 MPa and 333 K. The density of liquids is highly dependent on temperature and pressure and generally decreases with rising temperature as shown in Figs. 15.18 and 15.19. A number of authors have investigated the change in density for pure oils and fats as well as the change of their CO_2-saturated mixtures [28, 31, 32] as a function of pressure (Fig. 15.20). All these measurements have shown an increase in the pure triglyceride density at high pressures which is connected to a compression effect. Taking into account that in almost all measurements the pure CO_2 density was lower than the one of the liquid under pressure, it was surprising to find that the density of the CO_2-saturated triglycerides was higher than the pure oil as a function of pressure. Dittmar at al. [33] hypothesise that in a

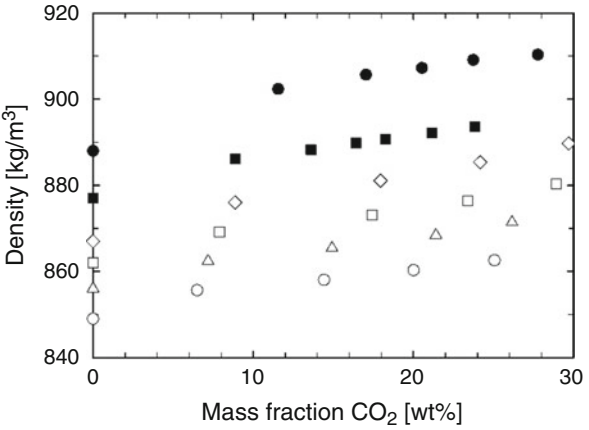

Fig. 15.21 Density of the CO_2-saturated triglycerides as a function of CO_2 solubility: tristearin (*open diamond*) 343 K, (*open square*) 353 K, (*open triangle*) 353 K and (*open circle*) 373 K; rapeseed oil (*filled circle*) 333 K and (*filled square*) 353 K

CO_2-saturated lipid, the CO_2 molecules can position themselves between the large lipid ones and therefore can act as a lubricant between them, increasing the compressibility of the lipid. Therefore, it can be expected that the amount of dissolved CO_2 plays a great role in the behaviour of the triglycerides density. The correlation of the density values for tristearin and rapeseed oil saturated with CO_2 to the gas solubility is presented in Fig. 15.21. The data show a linear increase in density with rising CO_2 solubility for both substances. Seifried and Temelli [31] could prove for fish oil that the CO_2 solubility only governs the density increase up to values as high as 25 wt%, above which this is influenced mainly by the compression of the mixture. This is indicated by a sharp uptake of the density with higher solubility. The same effect was observed in [28] for cocoa butter. In order to verify this effect for the triglycerides investigated in this work, further density measurements at higher pressures are needed. Unfortunately, the current apparatus used for this work can only be employed for measurements up to 20 MPa [13].

In comparison to the linear rise in density with increasing pressure and falling temperature for the triglycerides, no specific influence of pressure on the density of CO_2-saturated polymers could be observed as presented in Fig. 15.22. As the density of PEG 6000 shows light decrease, the density of the low molar mass polymer shows both, an increase and decrease with rising pressure. The original literature data for PEG 400 [20] shows high scatter of the results especially in the low pressure region, leading to high measuring uncertainties so that no further discussion on the influence of pressure on polymer density can be made.

Literature values for the density of CO_2-saturated water at temperatures between 313 and 374 K and pressures up to 20 MPa show linear increase with rising pressure for all isotherms (Fig. 15.23).

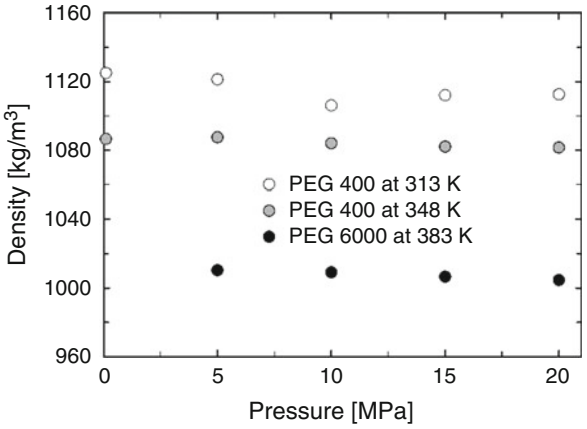

Fig. 15.22 Density of CO_2-saturated PEG 400 at 313 and 348 K [20] and CO_2-saturated PEG 6000 at 383 K [30] as a function of pressure

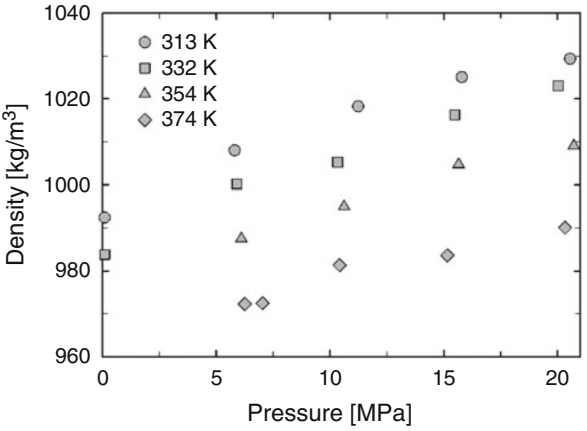

Fig. 15.23 Density of CO_2-saturated water as a function of pressure at 313, 332, 354 and 374 K [22]

15.3.2.4 Interfacial Tension

The interfacial tension of tristearin and rapeseed oil saturated with CO_2 up to pressures of 20 MPa are presented in Figs. 15.24 and 15.25, respectively. The isotherms for both triglycerides show a decrease in interfacial tension with rising pressure. For tristearin, a decrease from initial values of 27.6 to 28.8 mN/m at atmospheric pressure to 4.1, 4.7 and 5.2 mN/m at 20 MPa and 353, 363 and 373 K, respectively, was measured. In the case of rapeseed oil, the interfacial tension decreased from 29.8 to 31.3 mN/m at atmospheric pressure to 2.9 and 4.0 mN/m at 20 MPa and 333 and 353 K, respectively. The interfacial tension for both triglycerides decreases with rising temperature at pressures higher than 5 MPa, whereas at atmospheric pressure the highest value was measured at the lowest temperature. The inverted dependence of the interfacial tension on temperature as a function of pressure leads to a crossover in the isotherms. This effect has been

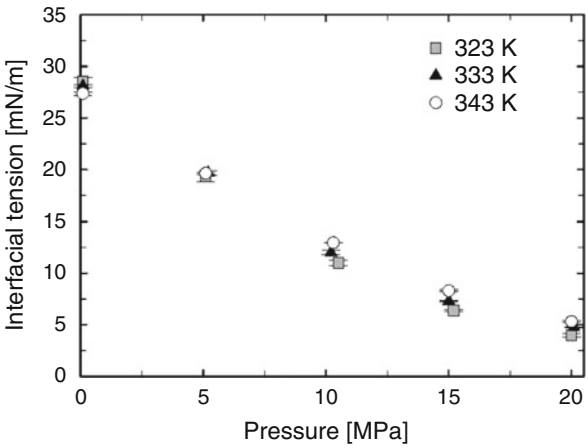

Fig. 15.24 Interfacial tension of tristearin and CO_2 as a function of pressure at 353, 363 and 373 K

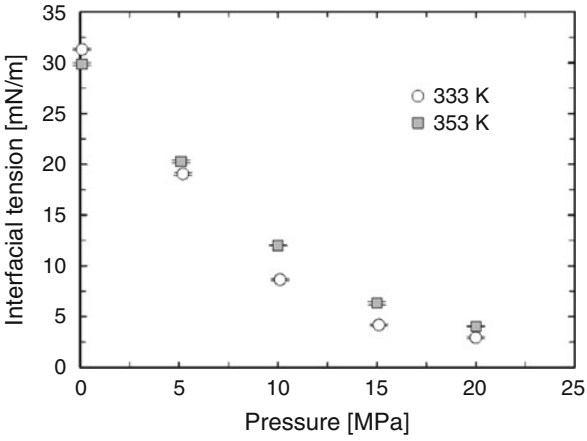

Fig. 15.25 Interfacial tension of rapeseed oil and CO_2 as a function of pressure at 333 and 353 K

observed also for other triglycerides in the literature. Seifried and Temelli [34] showed that for fish oil triglycerides, the crossover happens around 2.5 MPa, whereas Schiemann et al. [35] found this to be true around 2.8 MPa for olive oil. Dittmar et al. [36] compared the interfacial tension as a function of temperature and pressure for different vegetable oils saturated with CO_2 and noticed that all the oils showed the same values for the interfacial tension suggesting that the latter is independent of the triglyceride mixture. To further investigate this, the values obtained in this work for tristearin and rapeseed oil were plotted against literature values for corn germ oil taken from [36]. Figure 15.26 shows the interfacial tension of various oils as a function of pressure at 353 K. As previously stated, it can be observed that the interfacial tension of the plotted oils is not dependant on the composition of the triglyceride mixtures [13].

Figure 15.27 shows the correlation of the interfacial tension of tristearin and rapeseed oil, respectively, with the corresponding CO_2 density. An exponential

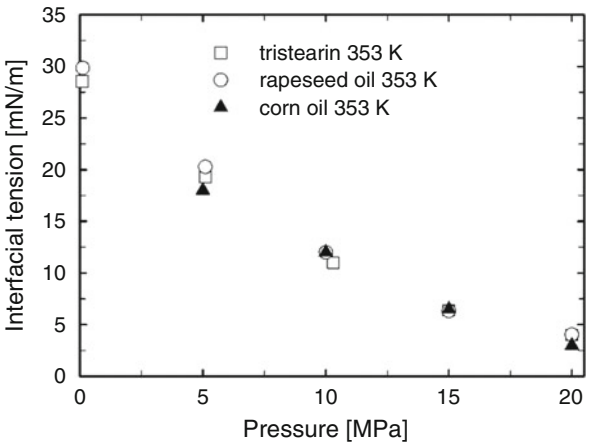

Fig. 15.26 Comparison of the interfacial tension of CO_2-saturated tristearin, rapeseed oil and corn oil [36] as a function of pressure

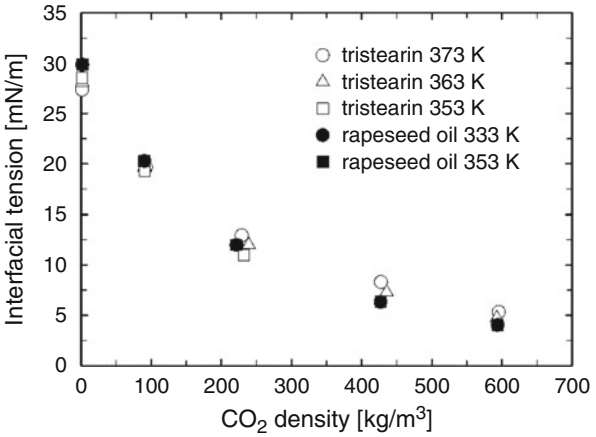

Fig. 15.27 Interfacial tension of CO_2-saturated tristearin and rapeseed oil as a function of CO_2 density

decrease of the interfacial tension for all isotherms and substances can be observed with rising CO_2 density. Moreover by doing so, Seifried and Temelli [34] observed for fish oil triglycerides a second crossover point of the isotherms at CO_2 densities around 600–700 kg/m^3 and correlated this with the change in CO_2 density which weakens above values of 600 kg/m^3. Unfortunately, the measurements in this work could only be carried out up to pressures of 20 MPa which corresponds to a CO_2 density of around 600 kg/m^3. Even so, it can be observed from Fig. 15.27 that the isotherms, which are clearly separated at lower densities, start to approach each other again around 600 kg/m^3 reaching near identical values. Therefore, it can be expected that at higher density values also for tristearin and rapeseed oil, a second crossing of the isotherms will occur [13].

Selected literature data for the relevant pressure and temperature range for the interfacial tension of PEG 400 [37] and PEG 6000 [30] and carbon dioxide are presented in Fig. 15.28. As expected the interfacial tension of both polymers

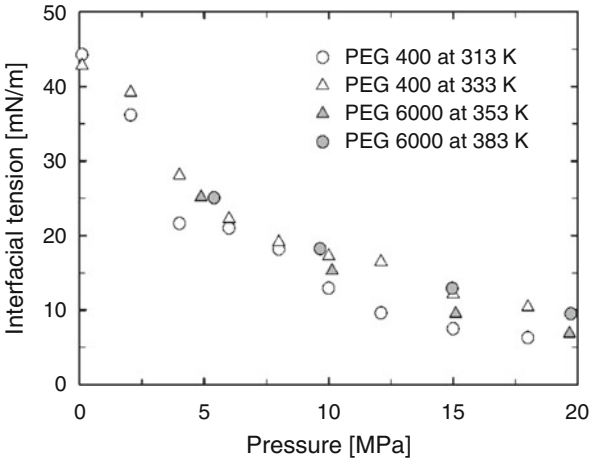

Fig. 15.28 Interfacial tension of PEG 400 and CO_2 at 313 and 333 K [37] and PEG 6000 and CO_2 at 353 and 383 K [30] as a function of pressure

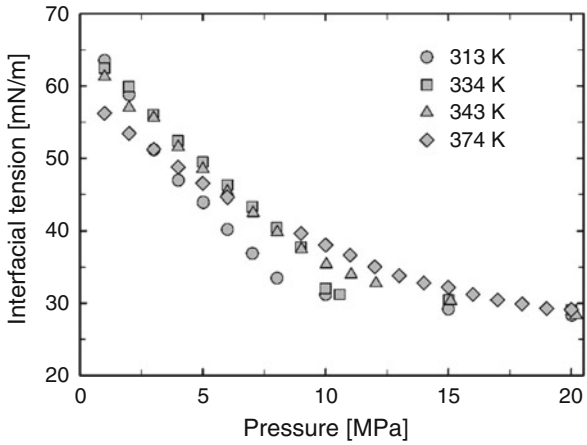

Fig. 15.29 Interfacial tension of water and CO_2 as a function of pressure at 313, 334, 343 and 374 K [10]

decreases with rising pressure. The crossover in the isotherms with increasing pressure can be observed also for PEG 400, although the correspondent pressure value for the crossover seems to be lower than 2.5 MPa. After this pressure, the interfacial tension of both polymers decreases with falling temperature, reaching values just around 6 mN/m for PEG 400 at 313 K and PEG 6000 at 353 K .

The same trend can be observed for water and carbon dioxide in Fig. 15.29. The crossover point of the isotherms is around 3 MPa, so the interfacial tension starts to decrease with increasing pressure and falling temperature until around 20 MPa where the all isotherms approach each other to a value of around 30 mN/m.

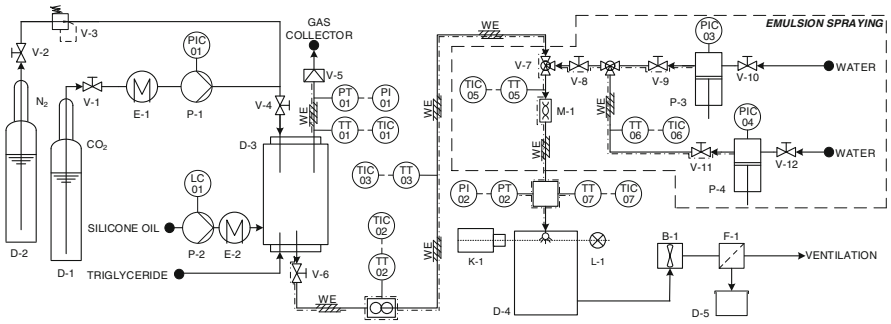

Fig. 15.30 Schematic flow chart of the apparatus used for spraying pure and gas-saturated substances and emulsions

15.3.3 Spray Behaviour and Powder Production

15.3.3.1 Experimental Procedure

The apparatus used for spraying pure and gas-saturated substances as well as emulsions is presented in Fig. 15.30. To avoid blockages in the apparatus due to material solidification all of its components were heated to the operating temperature. A minimum of 0.8 dm^3 of the substance to be sprayed was filled into a high-pressure autoclave (D-3).[1] The materials, which were solid at room temperature, were melted prior to the experiments. Subsequently carbon dioxide was added to the desired pressure using a high-pressure pump (P-1) equipped with a cooler (E-1, New Ways of Analytics). The temperature in the autoclave and at various points of the apparatus was measured by a K-type thermocouple and the pressure was measured by pressure gauge (Dynisco MDA420 $\pm 0.5\,\%$). The same procedure as for the phase equilibria measurements explained above was followed for the pre-saturation of the substances with carbon dioxide. The autoclave was put in its shaking position and this was carried out for at least 1 h, followed by a resting time of 1 h, to allow for the phases to separate. The spray tower was fixed underneath the nozzle (D-4) and the ventilation (B-1) was connected.

In some experiments, the spraying and saturation pressure were not identical. In those cases, the pressure was raised from the saturation one (P_{SAT}) to the desired spraying pressure (P_{SPRAY}) by adding gaseous nitrogen from a gas cylinder (D-2). The desired spraying pressure was set constant using a pressure regulator (V-3) connected to the nitrogen bottle. This is better explained using Fig. 15.31, where an example of the process is qualitatively shown in a phase diagram of an example substance and carbon dioxide. Firstly, the liquid or liquefied substance is saturated with carbon dioxide until the desired saturation pressure, P_{SAT} and after that,

[1] In the course of this work, two different autoclaves were used: a 1.3 dm^3 one for maximum 25 MPa and 473 K and 4.3 dm^3 one for maximum 40 MPa and 573 K.

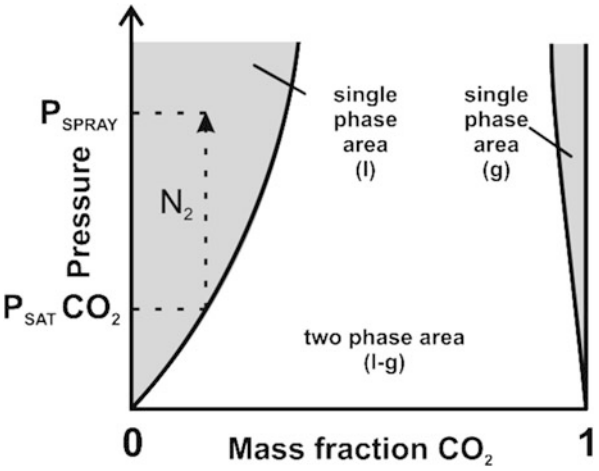

Fig. 15.31 Qualitative plot of the saturation process in a phase diagram of an example substance and carbon dioxide

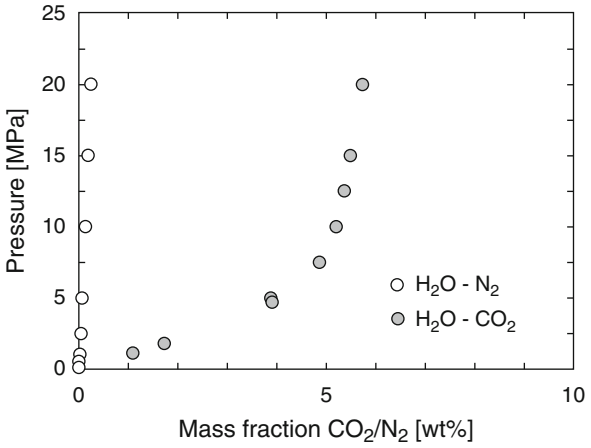

Fig. 15.32 Phase composition diagram of water and carbon dioxide [15, 38] and water and nitrogen [39] as a function of pressure

nitrogen is added until the spraying pressure, P_{SPRAY} is reached. Thus, sprays with different percentages of carbon dioxide at comparable spraying pressure could be realised. The nitrogen was added shortly before the spraying experiment. Its solubility in the sprayed substances is much lower than the one of carbon dioxide (Fig. 15.32, [15, 38, 39]). Also, the contact time of less than 1 h is short in comparison to the rate of diffusion within a liquid stagnant layer. Considering the two previous facts, it can be safely assumed that within the short time of less than 1 h, the experiment will not be seriously influenced by the adding of nitrogen. Additionally, the pure substances were sprayed without any saturation with carbon dioxide, only by pressurisation by gaseous nitrogen.

By opening the outlet valve at the bottom of the autoclave (V-6), the CO_2-saturated substance flows through the fan spray orifice as a result of the difference in pressure between the autoclave and the atmosphere. For the spraying of the pure

and gas-saturated substances, a BETE® BJH 0.33 mm flat fan orifice was used. The spraying angle was 20°. Depending on the flow characteristics a spray can be formed and is collected in a spray tower (D-4). Depending on the substances' melting point and the temperature in the spray tower, either droplets or a solid powder are collected. Images of the spray were taken with the help of a PIV capable system (particle image velocimetry, LaVision). Therefore, a short light pulse (L-1, Evergreen 145 Nd:YAG laser, 532 nm, 145 mJ) at 532 nm is transferred to a diffusor with a diameter of 120 mm. During the light pulse, a sCMOS-camera (K-1, Imager, LaVision) placed vis-à-vis to the diffusor takes a picture of the illuminated spray. Because of the short time light pulse, the structures of the spray are 'frozen' on the picture. These were taken directly under the nozzle with a dimension of 20 mm × 20 mm.

This same procedure was followed in the experiments where emulsions were sprayed. The substance which was filled in the autoclave is in this case the shell material, that is the continuous phase. The core material (dispersed phase) was filled in the syringe pumps (P-3, P-4) and heated up to the operating temperature, during the equilibration time of the continuous phase and carbon dioxide. The desired volume flow was set on the pump's control menu. By varying the latter, experiments with emulsions with different concentrations of the dispersed phase could be carried out. The spraying experiment was started with the simultaneous opening of the outlet valves of the autoclave (V-7) and syringe pump (V-8). The mass flow of the saturated shell material was governed by the pressure drop at the nozzle, so that it could only be indirectly influenced by variation of the spraying pressure. A Coriolis type mass flow meter (RHM04/RHE08, Rheonik Messtechnik GmbH, Germany) positioned directly after the opening valve of the autoclave was used to measure the flow of the gas-saturated shell material. The Coriolis mass flow mater can work with gasses or liquids, a homogenous one phase flow is however required for reliable results. Therefore, as a precautious measure the spraying pressure on the nitrogen bottle was always set a bit higher than the actual saturation pressure to ensure that no degasification occurs due to sudden pressure drop in the autoclave. To verify this, using the Bernoulli equation the total mass flows of the experiments have been calculated and compared with the experimentally determined ones. A cross-sectional change between the tube and the orifice was considered in the Bernoulli equation, the density corresponded to the one of the gas-saturated liquid at high pressure conditions. In the investigated temperature and pressure range, a maximum rise of 2 % in density with increasing pressure in comparison to ambient density was observed (Figs. 15.18, 15.19, 15.20, 15.21, 15.22 and 15.23), so that the restriction put on the Bernoulli equation coming from the constant density assumption could be fulfilled. This resulted in a good agreement with the experimentally determined flows. Following, it could be safely assumed that no degasification was present in the mass flow meter.

The gas-saturated shell and the core material are brought in contact in a tee piece (V-7) and forced under pressure through a static mixer (M-1) and a nozzle. An Agens® AMX static mixer with 12 mixing elements and a full length of 72 and

6 mm diameter was used. BETE® BJH flat fan orifice was used again for the spraying of the emulsions, with equivalent diameters ranging from 0.13 to 0.23 mm.

In an ideal case, a stable emulsion is created in the static mixer, which is then sprayed through the orifice. The pressure difference causes degasification of the CO_2 after the orifice, the gas expands and cools down due to the Joule–Thompson effect. The dissolving gas simultaneously promotes the breakup of the liquid and cools down the resulting droplets, ideally under the melting point of the shell material. The produced powder is collected in the spray tower (D-4) and the CO_2 is carried away by the ventilation.

15.3.4 Results

15.3.4.1 Disintegration of Pure and Gas-Saturated Liquid Sheets

The disintegration of liquid sheets as studied by many authors [40–42] is generally a two-step process. First, liquid threads and/or ligaments disintegrate from the sheet, which secondly break into droplets due to capillary instabilities. This can be induced either through perforations or destabilising waves in the liquid sheet [40].

If the liquid sheet disintegrates through perforations, holes appear on its surface, expand due to the contracting liquid surrounding them, coalesce and break off into threads. These break off further on into droplets. If, on the other hand, the reasons for sheet disintegration are waves on the surface, then fragments of the liquid sheet are torn off. These contract fast under surface tension, but might undergo further disintegration into droplets before a web of ligaments is created [40–42].

Adding gas to the liquid as it is the case in effervescent and flashing atomisation intensifies the first type of disintegration as the expanding gas after the nozzle ruptures the liquid sheet and promotes hole nucleation [42]. The difference between the previous gas-assisted atomisation processes and the one used in this work lays ultimately in the fact that 20–30 wt% of a dissolved supercritical fluid are present in the liquid prior to expansion. Moreover, choosing supercritical CO_2 as the assisting gas has other advantages. While adding any solvent to a liquid will result in a mixture with more or less changed properties, CO_2 as a non-toxic, non-flammable and inert gas tends to alter them to more favourable ones, as discussed above under thermodynamic properties of the liquid mixtures. It can be assumed that as in the case of effervescent and flash atomisation, the dissolved gas will promote the atomisation process. As after the nozzle the pressure equals the atmospheric one, the liquid becomes supersaturated so that CO_2 starts to outgas forming gas bubbles in the liquid sheet and initiating gas nucleation. The pre-expansion properties of the liquid start to change to match the ones at atmospheric pressure. As no previous research on the influence of high concentrations of dissolved gasses under high pressures on the breakup of liquid sheets has been done, the aim of this work is to investigate and determine differences to common disintegration mechanisms.

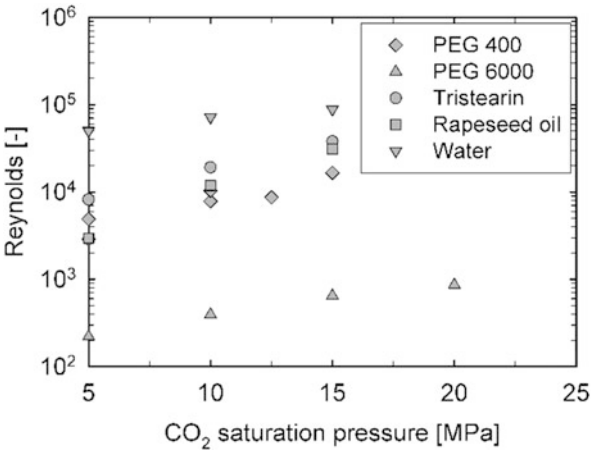

Fig. 15.33 Experimental Reynolds numbers as a function of CO_2-saturation pressure for the sprayed substances

The experiments have been carried out using the relevant model substances. As previously stated, each substance was sprayed pure and with different saturation degrees of CO_2 in order to investigate fundamental differences. Chosen experimental results are presented below. The spraying pressure was 15 MPa, unless indicated otherwise. This should help eliminate the differences in spray behaviour of the liquids coming from the high liquid sheet velocities rather than from the dissolved supercritical fluid. Great care is taken in choosing and setting the process parameters so that the mixture reaches the orifice as one and accordingly two phase flow in the case of emulsion. Figure 15.33 shows the experimental *Re* numbers at the orifice as a function of the CO_2 saturation pressure calculated according to (*15.1*),

$$Re = \frac{w \cdot d_N \cdot \rho_{Mix}}{\eta_{Mix}} \tag{15.1}$$

where w is the velocity of the fluid mixture after the nozzle calculated using the Bernoulli equation, d_N is the equivalent diameter of the nozzle and ρ_{Mix} and η_{Mix} are the density and viscosity of the mixture at 0.1 MPa and the spray temperature, respectively.

The pictures presented in Fig. 15.34 show the liquid sheet of water at 313 K and various spraying pressure, no CO_2 saturation. As already revealed, all images illustrate an area of 20 × 20 mm after the orifice.

The disturbances in the sheet intensify from left to right, moving the position of breakup of the lamella towards the orifice. The substantial difference in the liquid sheets presented in the above picture series is coming from the high velocity of the spray due to high injection pressures.

Comparing the set of pictures presented above with Fig. 15.35 shows the difference in the disintegration caused by the dissolved CO_2. An increase in holes/perforations, but not a significant decrease in breakup length, can be observed. The increased occurrence of holes is promoted from the nucleating

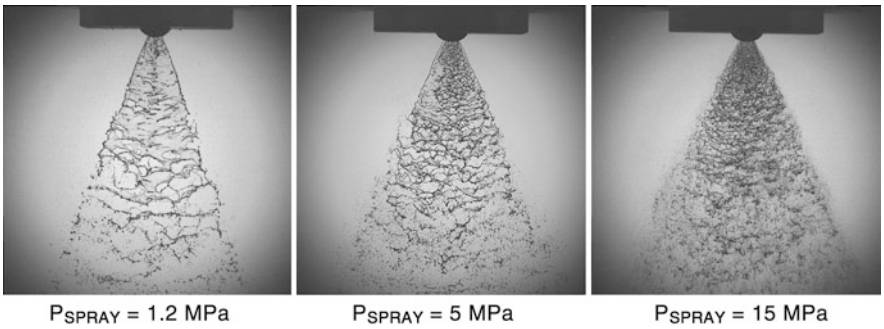

Fig. 15.34 Water at 313 K and different spraying pressures

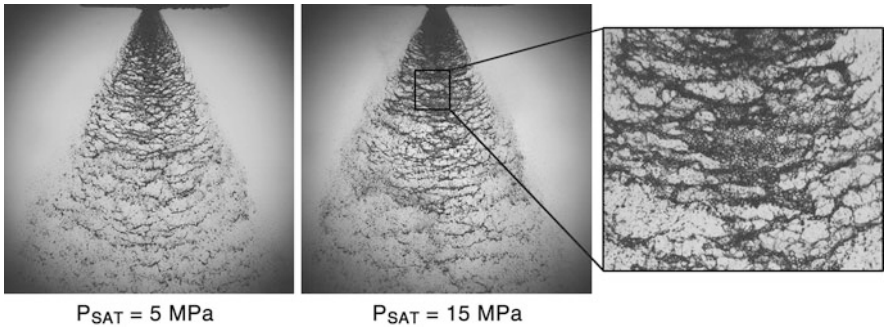

Fig. 15.35 CO_2-saturated water at 313 K and spraying pressure of 15 MPa

CO_2 as seen in the far right picture of Fig. 15.35 showing gas bubbles inside the liquid sheet.

No significant changes in density or viscosity of water can be attributed to the dissolved gas. Hence, the *Re* number of the water spray undergoes the least increase with rising saturation pressure, following Fig. 15.33. The surface tension of water is the only parameter that changes from 68 mN/m at 0.1 MPa to 32 mN/m at 15 MPa. Due to the higher surface tension and the corresponding high disturbance on the edges, no rim can be identified in both cases. Small droplets forming from threads on both sides of the lamella are present. The absence of a relevant difference in the sprays in Fig. 15.35 can be attributed to the fact that the CO_2 solubility in water is extremely low, rising from 5 wt% at 5 MPa, to 5.5 wt% at 15 MPa.

Figure 15.36 shows the disintegration of pure rapeseed oil at 1.2 and 15 MPa, no CO_2 saturation. In the investigated area, no perforations in the liquid sheet are visible. In both cases, a stable lamella with pronounced boundary rims can be observed. The spraying angle has widened with increasing pressure. In the lower region of the sheet, waves are visible. These are more pronounced at high pressure, due to the higher velocity of the liquid. Their presence usually leads to increased air friction, which eventually leads to a breakup of fragments of the liquid sheet and

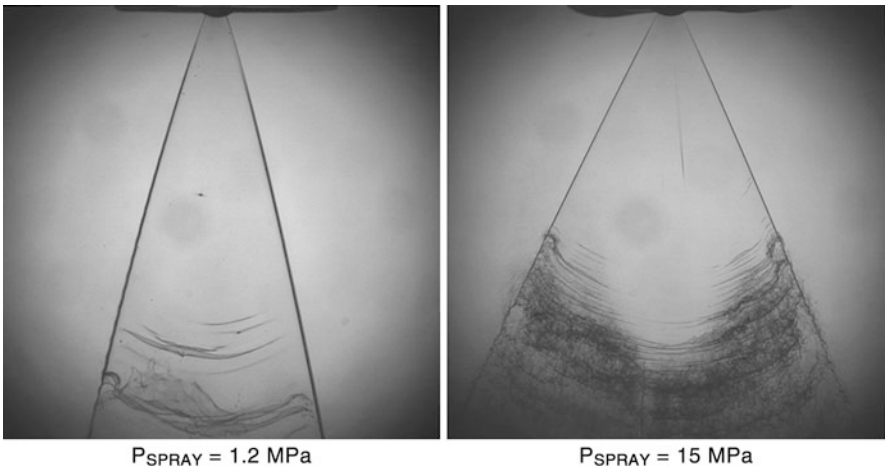

Fig. 15.36 Rapeseed oil at 313 K and different spraying pressures

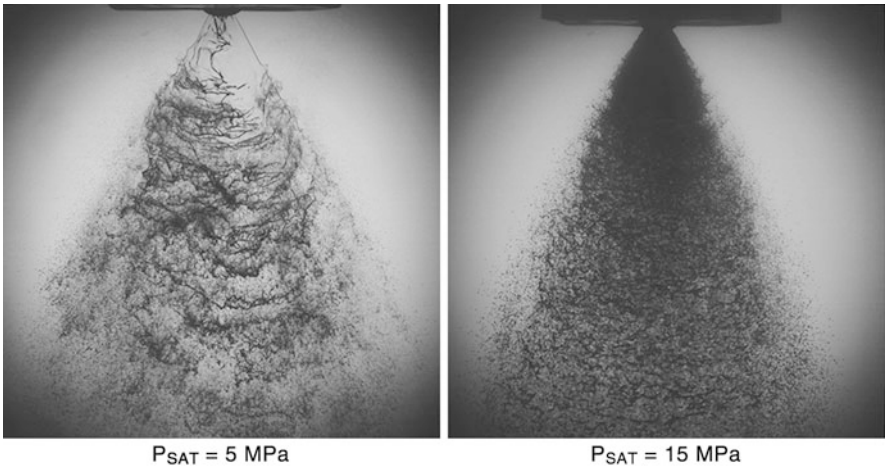

Fig. 15.37 CO_2-saturated rapeseed oil at 313 K and spraying pressure of 15 MPa

their subsequent breakup into droplets. However, the full disintegration of the liquid sheet into droplets is not observed in the investigated area.

Rapeseed oil has a much higher viscosity than water, namely 33 mPa s at 313 K and atmospheric pressure. Pre-saturating the oil with CO_2 reduces its viscosity, especially at 15 MPa following the diagram in Fig. 15.14. Comparing the pictures presented in Fig. 15.37 with the ones in Fig. 15.36, it can be observed that the stabile liquid sheet of the pure oil has been disturbed to the point of break up. Directly after the orifice a small area of highly disrupted sheet is formed (Fig. 15.37, P_{SAT} of 5 MPa), which does not develop to a greater extent due to

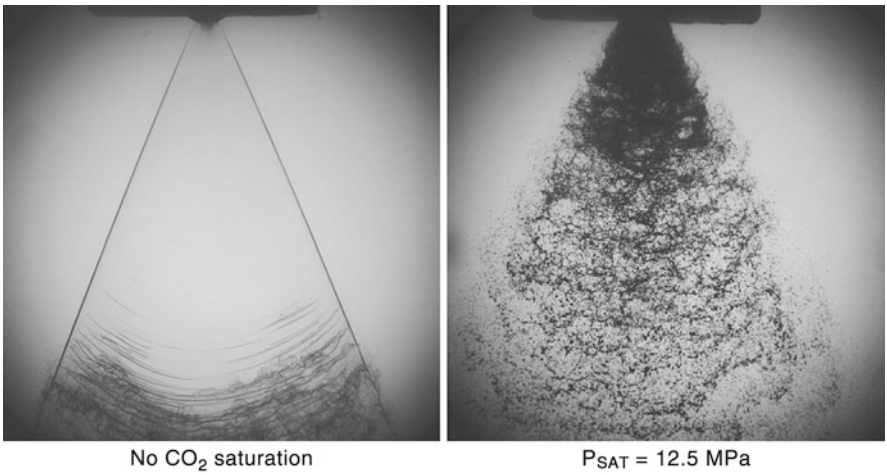

Fig. 15.38 Pure and CO_2-saturated PEG 400 at 313 K and spraying pressure of 15 MPa

expanding holes, which this time are promoted by the outgassing CO_2 bubbles. Due to the low surface tension, antennae are formed off the boundary rim, which account for small satellite droplets. Atomisation happens straight after/out of the orifice at 15 MPa, before a leading edge of the liquid sheet is even developed. The viscosity is reduced to under 2 mPa s and the saturation equals 27 wt%. Due to the high reduction of viscosity and increase in density with rising CO_2 saturation pressure, the *Re* number of the experiments with rapeseed oil changes the most increasing by factor ten from 5 to 15 MPa saturation.

Similarly as in the case of rapeseed oil, PEG 400 also demonstrates a higher liquid viscosity and therefore almost an identical spray as the one of pure rapeseed oil at 15 MPa, no CO_2 saturation (Figs. 15.36 and 15.38, respectively). Saturating the polymer with CO_2 at 12.5 MPa leads to increased instabilities in the near nozzle region promoted through gas bubble nucleation. Raising the temperature to 373 K and pre-saturating at 5 MPa to further decrease, the viscosity of the polymer (Fig. 15.39, left) leads to a spray that is nearly identical to the one of tristearin at 373 K and saturation pressure of 5 MPa (Fig. 15.40, left), as both substance exhibit similar properties at these conditions. Due to the high injection pressure (15 MPa) and hence high liquid velocities and increased aerodynamic friction, not only wave formation is promoted but also the resulting waves are shifted towards the nozzle, so that the disintegration happens before the sheet is fully formed. Decreasing viscosity further by saturating the substances with CO_2 at 15 MPa reveals significant difference (Fig. 15.39 right and Fig. 15.40 right) between the sprays.

The comparison of the shadowgraphs of rapeseed oil, PEG 400 and tristearin at saturation and spraying pressure of 15 MPa shows a difference in the spray which can be linked to the amount of dissolved CO_2, as the values of viscosity, density and interfacial tension are similar. At the highest saturation pressure, only 14 wt% gas is dissolved in the polymer, whereas 20 wt% is present in tristearin and 27 wt% in the vegetable oil. The breakup of the liquid sheet is now assisted by the CO_2 bubbles

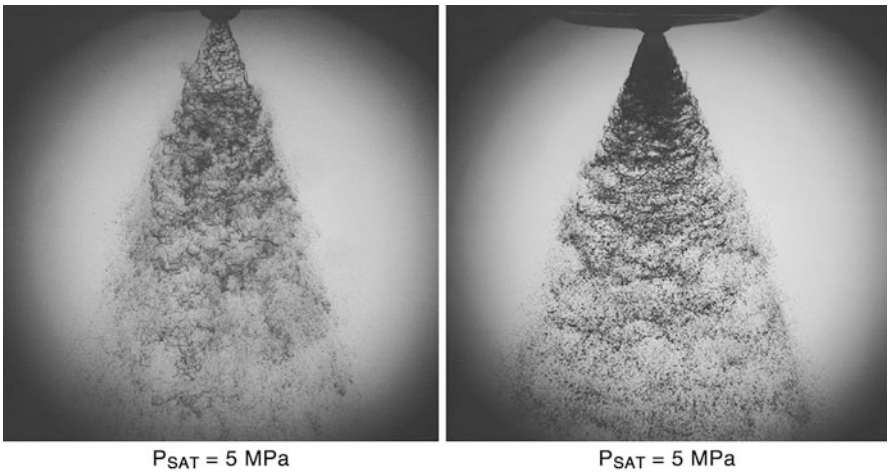

Fig. 15.39 CO_2-saturated PEG 400 at 373 K and spraying pressure of 15 MPa

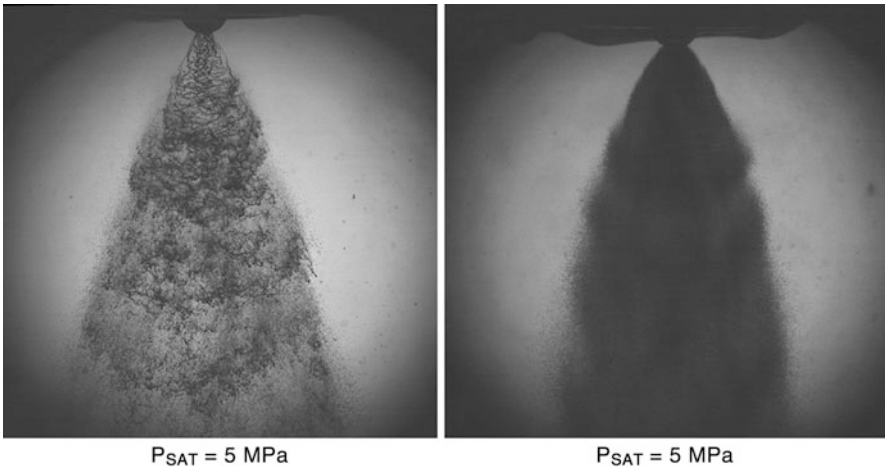

Fig. 15.40 CO_2-saturated tristearin at 373 K and spraying pressure of 15 MPa

forming inside the liquid, as at ambient pressure the liquid has suddenly become supersaturated with gas. These gas bubbles create additional holes in the sheet and since they appear close to the orifice they assist the atomisation process by shifting the position of disintegration further up. If enough CO_2 is dissolved, the liquid can be atomised straight after the orifice.

As theory has it, viscosity is responsible for stabilising liquid sheets and opposing any disturbances. This is clear from Fig. 15.41, where even at high injection pressures of 15 MPa, pure polyethylene glycol 6000 with a viscosity of ca. 500 mPa s produces a stable sheet, with thick rims at the end. Adding CO_2 to the polymer at 5 MPa lowers its viscosity to nearly half of the atmospheric value. Small gas

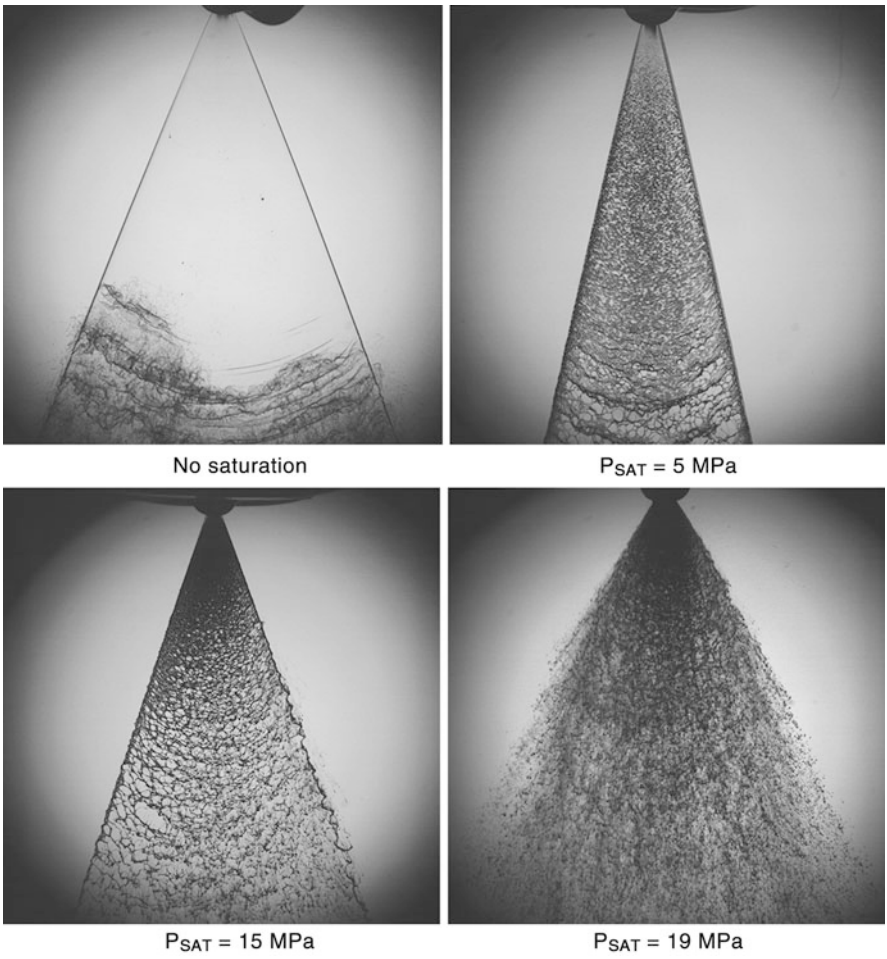

Fig. 15.41 Pure and CO_2-saturated PEG 6000 at 373 K and spraying pressure of 15 MPa

bubbles emerging inside the liquid can be seen, their coalescence and expansion seems to be hindered by the high viscosity of the liquid, so that perforations can only be observed far away from the orifice. Decreasing the viscosity even further while increasing the dissolved CO_2 amount in the polymer (p_{SAT} of 15 MPa) leads to an interesting effect. Straight after the nozzle high number of perforations can be observed in the sheet; nevertheless, the shape of the sheet has been preserved. The viscosity is opposing any instabilities coming from aerodynamic interaction, the sheet is disrupted solely by the dissolved gas. Gas bubbles most probably form straight after the nozzle, expand and perforate the sheet. A single network of connected threads and ligaments form the sheet throughout the whole length. The rims of the lamellae are only destabilised in the lower part of the sheet far away

from the nozzle. A further increase in saturation as well as spraying pressure to 20 MPa leads to a complete disintegration of the liquid sheet and droplet formation. The viscosity is further decreased by 20 mPa s and the CO_2 amount in the polymer increases by roughly 5 wt%. A combination of lower viscosity, surface tension and higher CO_2 amount in the liquid sheet in combination with higher injection pressure and therefore higher velocities, obviously promotes the breakup of the ligament network created at 15 MPa into droplets.

To summarise these results, the shadowgraphs were ordered in accordance to their liquid properties as shown in Fig. 15.43. The photographs of the sprayed substances are ordered in such a way that the CO_2 saturation increases for each substance from top to bottom. The viscosity of the pure as well as the gas-saturated liquids increases from left to right. The interfacial tension of the liquids against carbon dioxide decreases from right to left, with the exception of PEG 6000, whose interfacial tension values at 373 K and different CO_2 pressures fit between the ones of PEG 400 and tristearin. The interfacial tension changes from the maximum of 32 mN/m for water to 13 mN/m for rapeseed oil at 15 MPa and corresponding spray temperatures. The viscosity on the contrary increases from 0.7 mPa s for water to 117.8 mPa s for PEG 6000. The high viscosity difference between water and PEG 6000 could be assumed also from the pictures, as the liquid sheet of the polymer proves to be much more resistant to disintegration. Moreover, it is evident from Fig. 15.43 that with rising CO_2 saturation the disturbances on the liquid sheet are intensified and shifted towards the orifice, so that an earlier sheet breakup in comparison to the pure substances could be achieved.

To investigate the influence of a dispersed water phase on the sheet disintegration, experiments have also been carried out with concentrated water in oil emulsions. The concentration of the dispersed phase was varied between 0 and 50 wt% as was the saturation pressure. Rapeseed oil was used as a continuous oil phase, and water as a dispersed one. Figure 15.42 shows the disintegration of the emulsion at a saturation pressure of 5 MPa and 333 K. For better representations, the images have been cropped and only show an area after the nozzle of 12 mm $\times$ 32 mm.

It can be observed from the images that the stable rapeseed oil liquid sheet is significantly disturbed by the dispersed water phase at all concentrations. The breakup length of the liquid sheet is shortened as due to the dispersed water droplets the number of developing holes has increased. They seem to occur irregularly, causing random local perforations of various sizes inside the liquid sheet before its actual breakup. With increasing water concentration, the disturbance on the liquid sheet intensifies Fig. 15.42.

15.3.4.2 Powder Characteristics

In the scope of this project, experiments with two model emulsions and the CO_2-assisted high pressure spraying process are planned. So far, only experiments with water and tristearin have been carried out. No emulsifier was added previously to the substances and no premixing was carried out. The aim was to explore new

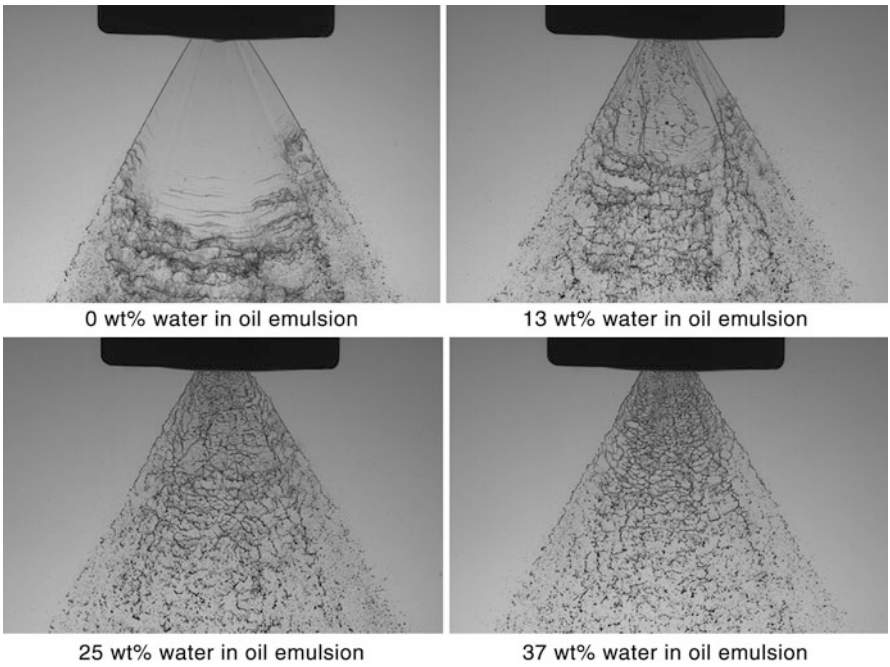

Fig. 15.42 Different concentrations of water in rapeseed oil emulsion at 313 K and 5 MPa

possibilities with the spraying process in which use would be made of the favourable properties of the CO_2-saturated liquids. As showed earlier in Fig. 15.26, the interfacial tension of the substances against carbon dioxide decreases with rising pressure. Since no literature data is available (measurements are being currently carried out by the authors), an assumption is made that this will also be the case for the surface energy of an interface between two immiscible liquids, such as water and oil when carbon dioxide is added. If this proves true, then adding an emulsifier to the mixture to lower the interfacial tension and hence to ease the emulsification process in the static mixer becomes an unnecessary step in the process. Moreover, by a variation of the saturation pressure of the continuous phase, its viscosity is directly influenced, allowing for fine tuning of the viscosity ratio between the two liquid phases.

The experiments have been carried out at two different temperatures, 353 and 373 K. At the higher temperature, however highly inhomogeneous particles were created. The 20 K difference corresponds to a couple of percent less dissolved CO_2 in the liquid so that the cooling effect of the surrounding gas will practically not change and therefore result in higher temperature differences between the liquid droplets and the gas atmosphere. Following, the solidification process of the droplets is prolonged and the possibility of coalescence and agglomeration increased. The temperature of 353 K proved to be optimal for the water and

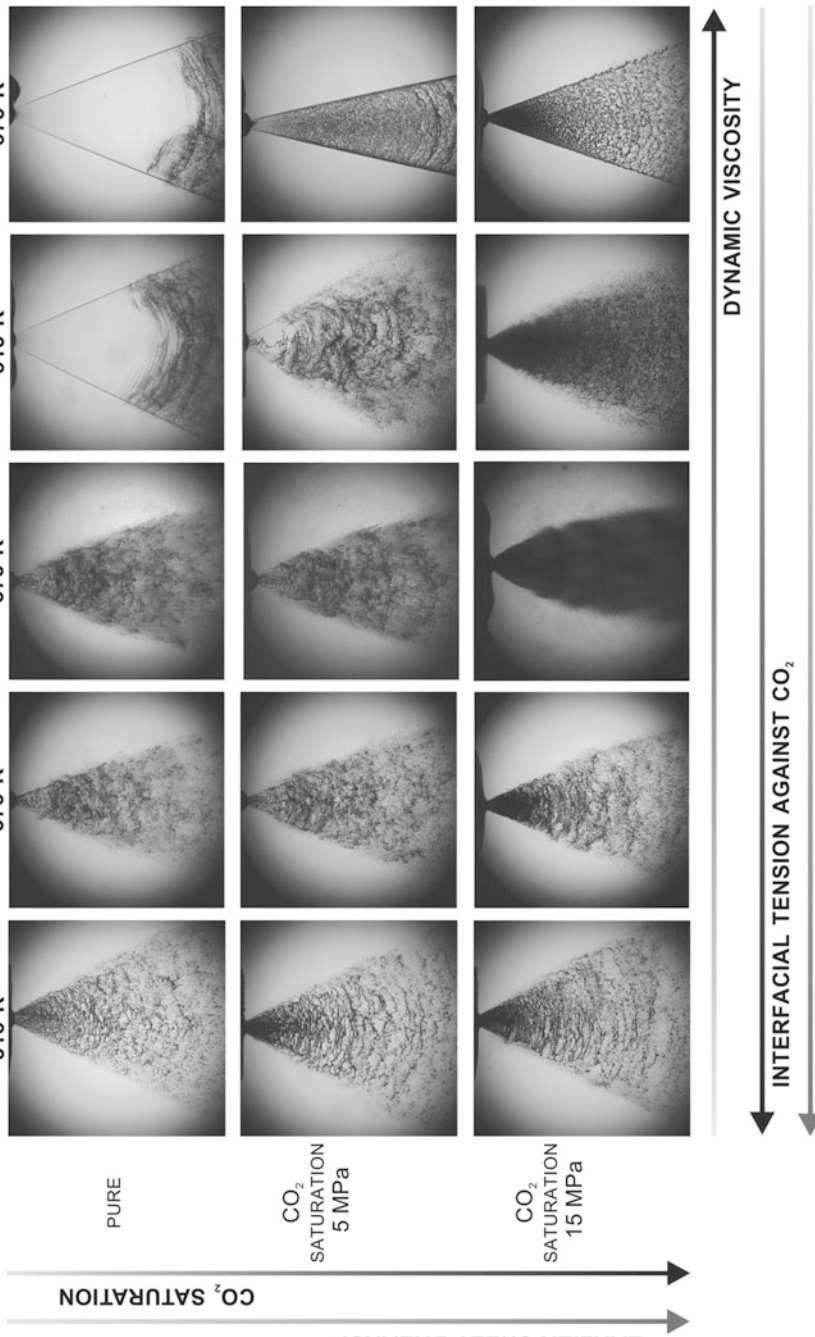

Fig. 15.43 Photographs of the disintegration of liquid sheets of pure substances and their CO_2-saturated mixtures as a function of saturation degree, dynamic viscosity and interfacial tension

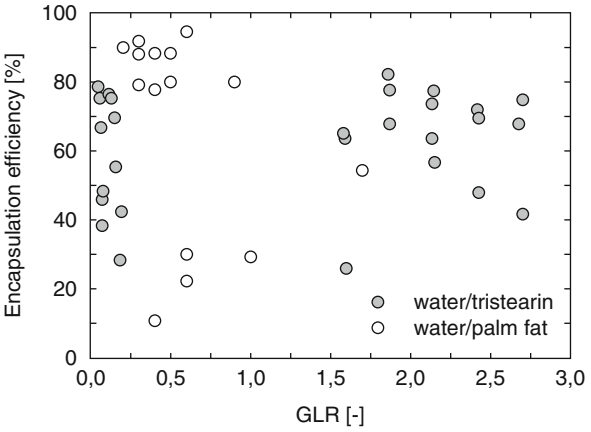

Fig. 15.44 Encapsulation efficiency as a function of the gas-to-liquid ratio

tristearin model emulsion, as an even lower temperature would provoke easily blockages in the pipes of the apparatus due to unwanted fat solidification.

The most important factor characterising the powder was its water content, which was measured using a halogen moisture analyser (HB43-S, Mettler Toledo GmbH, Germany). To account for this, the encapsulation efficiency of the experiments was calculated using (15.2) and the results are presented in Fig. 15.44.

$$\text{Encapsulation efficiency} = \frac{\text{Calculated water concentration in the emulsion}}{\text{Measured water concentration in the powder}} \quad (15.2)$$

The results for water and tristearin show encapsulation efficiencies between 25 and 80 %. Gas to liquid ratios (GLR) higher than 1.5 correspond to experiments where the amount of CO_2 added was higher than the saturation one, which resulted in an additional third fluid phase, but led to no improvement of the efficiency values. All powders had particle sizes in the range of 10 µm and mainly spherical morphologies as shown in Figs. 15.45 and 15.46, respectively, were produced.

The results were compared to literature ones, where water in palm fat emulsion with an emulsifier was sprayed [43]. The initial results achieved in this work without emulsifier show lesser encapsulation efficiencies, however not unsatisfactory ones, as they indicate that the presence of CO_2 is beneficiary for the production of solid water in oil emulsions. To further explore this effect, several factors that could influence the efficiency of the process were considered, amongst them, the quality of the emulsion and the corresponding droplets sizes of the dispersed phase.

To this end, a high-pressure view chamber was designed, which allows visual observation of the flow after the static mixer, presented in Fig. 15.47. The chamber is built of acrylic glass for pressures up to 10 MPa. The thickness of the inside channel was roughly 400 µm and the window size is 10 × 10 mm. First experiments carried out at a saturation pressure of 5.2 MPa, 353 K and a viscosity ratio of 0.7 show an influence of the static mixer Re (Re_{SM}) at otherwise identical parameters. The Re of the static mixer is calculated using (15.3), with parameters corresponding

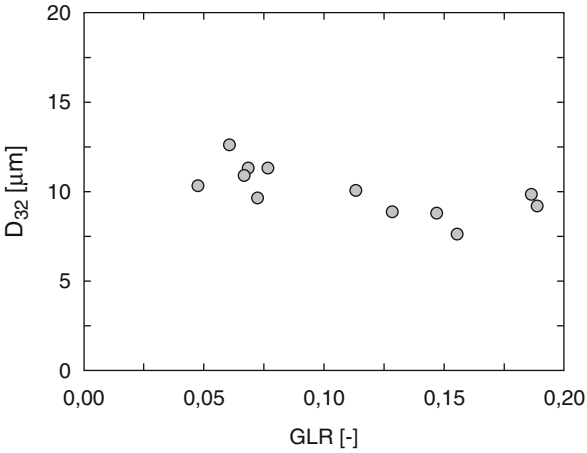

Fig. 15.45 Sauter mean diameter as a function of the GLR for the powders produced at 353 K

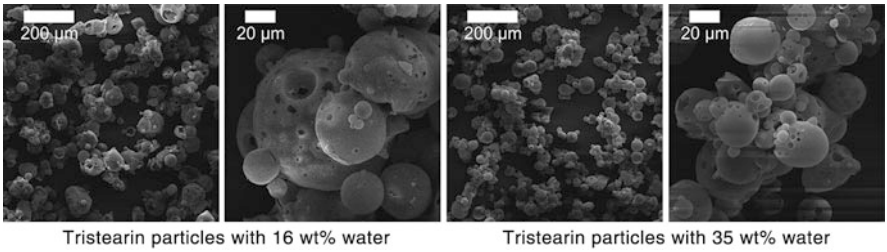

Fig. 15.46 SEM images of tristearin particles with different concentration of water

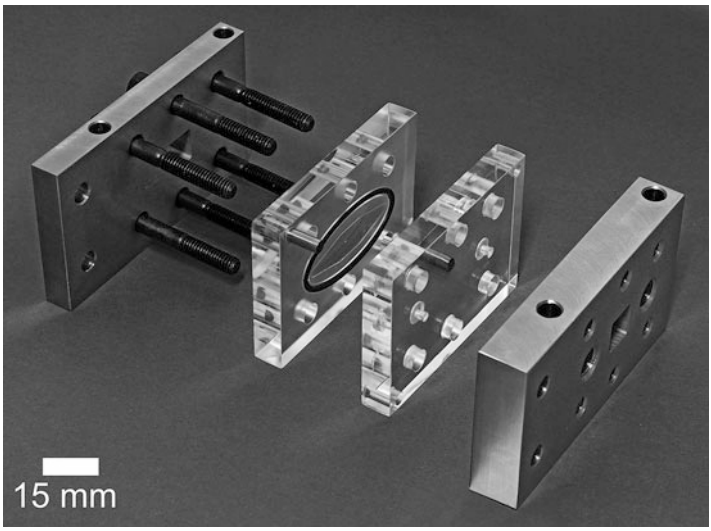

Fig. 15.47 High-pressure chamber for visual observation of the emulsion quality after the static mixer

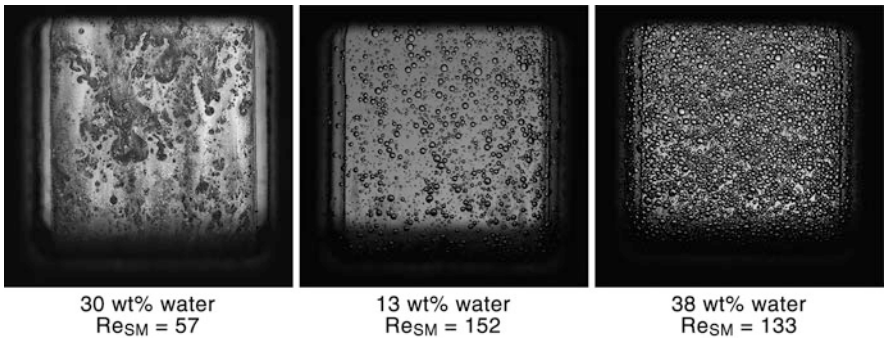

Fig. 15.48 Emulsion quality after the static mixer at 353 K and 5.2 MPa and different concentrations of the dispersed phase

to the flow before the expansion. The velocity w is calculated from the total mass flow of the mixture, D is the pipe inner diameter with consideration of a porosity factor ε of 0.78 and ρ_{Mix} and η_{Mix} are the density and viscosity of the mixture at the saturation pressure and temperature, respectively.

$$Re = \frac{w \cdot D \cdot \rho_{\mathrm{Mix}}}{\eta_{\mathrm{Mix}} \cdot \varepsilon} \tag{15.3}$$

Images of the emulsion quality are presented in the following Fig. 15.48. The left image shows that at Re_{SM} of 57 no droplet breakup in the static mixer is possible. Experiments carried out at similar conditions resulted in extremely wet powders, as due to the inhomogeneous mixture water was sprayed partly directly on the fat. Increasing the turbulence to Re_{SM} of double the previous value results in an emulsion with droplet size of maximum 350 µm.

The size of the dispersed drops is however higher than the used nozzle diameter of maximum 230 µm and the size of the produced powder particles, indicating that also the flow in the nozzle will have an influence on the end structure of the emulsion. Further experiments, where through variation of the saturation pressure and nozzle diameter, the GLR, Re_{SM} and the viscosity ratio are manipulated to find the optimal parameters for the emulsification process, are currently being carried out.

15.4 Conclusions

This project was started with the investigation of the thermophysical properties of the model substances as their knowledge was essential to understanding the fundamentals of the employed CO_2-assisted spraying process. To this end, fluid properties that are known to govern the spray and strongly influence the particle formation have been investigated in wide ranges of pressure and temperature, common for the

spraying process. This investigation was thereafter limited to solubility, density, viscosity and interfacial tension. It was shown that the solubility of the carbon dioxide increases with pressure and decreasing temperature. All investigated substances showed a negligent amount of solubility in carbon dioxide, on the contrary the gas dissolved in quantities of more than 30 wt% in some of the model substances such as rapeseed oil and tristearin. The viscosity of the CO_2 expanded liquids was also reduced in all cases. A maximum reduction of around 90 % was achieved again for rapeseed oil and tristearin. The density on the contrary showed a linear increase of up to 5 % with rising pressure and temperature. The interfacial tension of the liquids against carbon dioxide was also diminished to values under 10 mN/m with rising pressure and falling temperature, except for water where with the property could be reduced to around 30 mN/m.

The properties were used to explain the differences in the disintegration mechanisms of liquid sheets of pure and gas-saturated liquids. It was showed that carbon dioxide promotes the destabilisation of the liquid sheets with varying intensity. The latter was linked to the saturation pressure, as this directly influences the amount of dissolved CO_2 as well as the reduction of viscosity and interfacial tension. The disintegration of liquid sheets was promoted through an increased number of perforations occurring in the lamellae close to the nozzle. This was caused by the nucleating CO_2 due to the high pressure difference before and after the orifice. Further on, it was shown that at otherwise similar properties, the amount of CO_2 plays a key role in the intensity of the disturbances it causes on the liquid sheet. Both rapeseed oil and tristearin could be atomised after the orifice in comparison to polyethylene glycol, where at similar conditions a sheet with short intact length was still formed. Moreover, it was shown that by increasing the saturation pressure to lower the high viscosity of the polymer, atomisation could be achieved in comparison to the otherwise stable sheet of the pure polymer in the observed area after the nozzle. Adding a second dispersed liquid phase decreased further on the breakup length of the liquid sheet. This was investigated using various concentrations of water in rapeseed oil. Higher concentration of the dispersed phase caused an increased number of perforations.

The production of solid emulsion powders was successfully carried out. Powders consisting of tristearin and water concentrations of up to 35 wt% were produced without using an emulsifier with particles sizes in the range of 10 µm were produced. It was observed that the supercritical fluid can act as an emulsifier to lower the interfacial tension between the dispersed and continuous phase. A visual investigation of the emulsion quality showed improvement of the latter with increasing turbulence in the static mixer. It was observed however that the structure of the produced emulsion will be most probably affected by the nozzle flow. Ongoing experiments where a variation of the saturation pressure, nozzle diameter, and viscosity ratio should help link the droplet sizes to dimensionless numbers and determine the optimal parameters for the encapsulation process.

Acknowledgements The authors wish to thank the German Research Foundation (DFG) for financing this work within SPP1423 Process Spray.

References

1. Jung, J., & Perrut, M. (2001). Particle design using supercritical fluids: Literature and patent survey. *Journal of Supercritical Fluids, 20*, 179–219.
2. Weidner, E. (2009). High pressure micronization for food applications. *Journal of Supercritical Fluids, 47*, 556–565.
3. Knez, Ž., Markočič, E., Leitgeb, M., Primožič, M., Knez Hrnčič, M., & Škerget, M. (2014). Industrial applications of supercritical fluids: A review. *Energy, 77*, 235–243.
4. Reverchon, E., Adami, R., Campardelli, R., Della Porta, G., de Marco, I., & Scognamiglio, M. (2015). Supercritical fluids based techniques to process pharmaceutical products difficult to micronize: Palmitoylethanolamide. *Journal of Supercritical Fluids, 102*, 24–31.
5. Kalähne, A. (1914). Die Frequenzänderung schwingender Saiten und Stäbe in Flüssigkeiten und Gasen. *Annalen der Physik, 351*, 1–38.
6. Tropea, C., Yarin, A. L., & Foss, J. F. (2007). *Springer handbook of experimental fluid mechanics*. Berlin: Springer.
7. Viswanath, D. S., Ghosh, T., Prasad, D. H. L., Dutt, N. V. K., & Rani, K. Y. (2007). Viscosity of liquids: Theory, Estimation, Experiment and Data. Dordrecht: Springer.
8. Andreas, J. M., Hauser, E. A., & Tucker, W. B. (1938). Boundary tension by pendant drops. *Journal of Physical Chemistry, 42*, 1001–1019.
9. Hebach, A., Oberhof, A., Dahmen, N., Kögel, A., Ederer, H., & Dinjus, E. (2002). Interfacial tension at elevated pressures—Measurements and correlations in the water + carbon dioxide system. *Journal of Chemical & Engineering Data, 47*, 1540–1546.
10. Georgiadis, A., Maitland, G., Trusler, J. P. M., & Bismarck, A. (2010). Interfacial tension measurements of the ($H_2O + CO_2$) system at elevated pressures and temperatures. *Journal of Chemical & Engineering Data, 55*, 4168–4175.
11. Weber, W., Petkov, S., & Brunner, G. (1999). Vapour–liquid-equilibria and calculations using the Redlich–Kwong-Aspen-equation of state for tristearin, tripalmitin, and triolein in CO_2 and propane. *Fluid Phase Equilibria, 158–160*, 695–706.
12. Perko, T., Knez, Ž., & Škerget, M. (2012). Phase equilibria of glycerol tristearate and glycerol trioleate in carbon dioxide and sulfur hexafluoride. *Journal of Chemical & Engineering Data, 57*, 3604–3610.
13. Ilieva, P., Kilzer, A., & Weidner, E. (2015). Measurement of solubility, viscosity, density and interfacial tension of the systems tristearin and CO_2 and rapeseed oil and CO_2. *Journal of Supercritical Fluids* (03 May 2016, In Review).
14. Klein, T., & Schulz, S. (1989). Measurement and model prediction of vapor-liquid equilibria of mixtures of rapeseed oil and supercritical carbon dioxide. *Industrial & Engineering Chemistry Research, 28*, 1073–1081.
15. Wiebe, R., & Gaddy, V. L. (1939). The solubility in water of carbon dioxide at 50, 75 and 100° at pressures to 700 atmospheres. *Journal of the American Chemical Society, 61*, 315–318.
16. Hou, S.-X., Maitland, G. C., & Trusler, J. M. (2013). Measurement and modeling of the phase behavior of the (carbon dioxide + water) mixture at temperatures from 298.15 K to 448.15 K. *Journal of Supercritical Fluids, 73*, 87–96.
17. Kukova, E. (2003). *Phasenverhalten und Transporteigenschaften binärer Systeme aus hochviskosen Polyethylenglykolen und Kohlendioxid*. PhD Thesis, Bochum.
18. Wiesmet, V. (1998). *Phasenverhalten binärer Systeme aus Polyethylenglykolen, Polyglykoldimethylethern und verdichteten Gasen*. PhD Thesis, Erlangen.
19. Hrnčič, M. K., Škerget, M., & Knez, Ž. (2014). Density and viscosity of the binary polyethylene glycol/CO_2 systems. *Journal of Supercritical Fluids, 95*, 641–668.
20. Gourgouillon, D., Avelino, H. M. N. T., Fareleira, J. M. N. A., & Nunes da Ponte, M. (1998). Simultaneous viscosity and density measurement of supercritical CO_2-saturated PEG 400. *Journal of Supercritical Fluids, 13*, 177–185.
21. Verein Deutscher Ingenieure, VDI-Wärmeatlas. (2006). *[Berechnungsunterlagen für Druckverlust, Wärme- und Stoffübertragung]*. Berlin: Springer.

22. Dittmar, D. (2008). *Untersuchungen zum Stofftransport über Fluid-Flüssig Phasengrenzen in Systemen unter erhöhten Drücken*. PhD Thesis. Aachen: Shaker.
23. Fasinaa, O. O., Hallmanb, H., Craig-Schmidt, M., & Clementsa, C. (2006). Predicting temperature-dependence viscosity of vegetable oils from fatty acid composition. *Journal of American Oil Chemistry Society, 83*, 899–903.
24. Ceriani, R., Paiva, F. R., Gonçalves, C. B., Batista, E. A. C., & Meirelles, A. J. A. (2008). Densities and viscosities of vegetable oils of nutritional value. *Journal of Chemical & Engineering Data, 53*, 1846–1853.
25. Noureddini, H., Teoh, B. C., & Davis Clements, L. (1992). Viscosity of vegetable oils and fatty acids. *Journal of American Oil Chemistry Society, 69*, 1189–1191.
26. Jenab, E., & Temelli, F. (2011). Viscosity measurement and modeling of canola oil and its blend with canola stearin in equilibrium with high pressure carbon dioxide. *Journal of Supercritical Fluids, 58*, 7–14.
27. Seifried, B., & Temelli, F. (2011). Viscosity and rheological behaviour of carbon dioxide-expanded fish oil triglycerides: Measurement and modeling. *Journal of Supercritical Fluids, 59*, 27–35.
28. Calvignac, B., Rodier, E., Letourneau, J.-J., Almeida dos Santos, P. M., & Fages, J. (2010). Cocoa butter saturated with supercritical carbon dioxide: Measurements and modelling of solubility, volumetric expansion, density and viscosity. *International Journal of Chemical Reactor Engineering, 8*, 1–29.
29. Hobbie, M. (2006). *Bildung von Tropfen in verdichteten Gasen und stationäre Umströmung fluider Partikel bei Drücken bis zu 50 MPa*. PhD Thesis. Düsseldorf: VDI-Verlag.
30. Brinkmann, J. (2013). *Aufbau und Validierung von in-situ-Messmethoden für den Hochdruckbereich Phasenverhalten, Dichten, Viskositäten und Grenzflächenspannungen des Modellsystems Polyethylenglycol, Wasser und Kohlenstoffdioxid*. PhD Thesis. Bochum.
31. Seifried, B., & Temelli, F. (2009). Density of marine lipids in equilibrium with carbon dioxide. *Journal of Supercritical Fluids, 50*, 97–104.
32. Tegetmeier, A. (2000). Density and volume of water and triglyceride mixtures in contact with carbon dioxide. *Chemical Engineering and Processing, 39*, 399–405.
33. Dittmar, D., de Arévalo, A. M., Beckmann, C., & Eggers, R. (2005). Interfacial tension and density measurement of the system corn germ oil—Carbon dioxide at low temperatures. *European Journal of Lipid Science and Technology, 107*, 20–29.
34. Seifried, B., & Temelli, F. (2010). Interfacial tension of marine lipids in contact with high-pressure carbon dioxide. *Journal of Supercritical Fluids, 52*, 203–214.
35. Schiemann, H., Weidner, E., & Peter, S. (1993). Interfacial tension in binary systems containing a dense gas. *Journal of Supercritical Fluids, 6*, 181–189.
36. Dittmar, D., Kahl, H., Enders, S., & Eggers, R. (2002). Measurement and modelling of the interfacial tension of triglyceride mixtures in contact with dense gases. *Chemical Engineering Science, 57*, 355–363.
37. Hrnčič, M. K., Kravanja, G., Škerget, M., Sadiku, M., & Knez, Ž. (2015). Investigation of interfacial tension of the binary system polyethylene glycol/CO_2 by a capillary rise method. *Journal of Supercritical Fluids, 102*, 9–16.
38. Kiepe, J., Horstmann, S., Fischer, K., & Gmehling, J. (2002). Experimental determination and prediction of gas solubility data for $CO_2 + H_2O$ mixtures containing NaCl or KCl at temperatures between 313 and 393 K and pressures up to 10 MPa. *Industrial & Engineering Chemistry Research, 41*, 4393–4398.
39. Sun, R., Hu, W., & Duan, Z. (2001). Prediction of nitrogen solubility in pure water and aqueous NaCl solutions up to high temperature, pressure, and ionic strength. *Journal of Solution Chemistry, 30*, 561–573.
40. Fraser, R. P., Eisenklam, P., Dombrowski, N., & Hasson, D. (1962). Drop formation from rapidly moving liquid sheets. *American Institute of Chemical Engineers Journal, 8*, 672–680.

41. Dombrowski, N., & Fraser, R. P. (1954). A Photographic investigation into the disintegration of liquid sheets. *Philosophical Transactions of the Royal Society A: Mathematical, Physical and Engineering Sciences, 247*, 101–130.
42. Lefebvre, A. H. (1989). *Atomization and sprays*. New York: Taylor & Francis.
43. Hanu, L. G. (2010). *Manufacturing and characterization of water filled microcomposites obtained by the PGSS process*. PhD Thesis. Bochum.